Correspondence to:

A. A. Morrison,
aaron.a.morrison@gmail.com

A Reevaluation of Cryolava Flow Evolution: Assumptions, Physical Properties, and Conceptualization

Aaron A. Morrison[1] , **Alan G. Whittington[1]**, and **Karl L. Mitchell[2]**

[1]Department of Geological Sciences, The University of Texas at San Antonio, San Antonio, TX, USA, [2]Jet Propulsion Laboratory, California Institute of Technology, Pasadena, CA, USA

Abstract Cryovolcanism has been invoked to explain numerous features observed on icy bodies. Many of these features show similar morphologies to volcanic features observed on Earth suggesting similar physics involved in their formation. Cryovolcanism lies at the intersection of volcanology and hydrology but as such, no one model from either discipline satisfactorily represents cryolava flow emplacement. We produced a new model for cryolava flow evolution that draws from both disciplines to track the physical, chemical, and thermal states of a hypothetical H_2O-NaCl flow on a Europa-like body as it evolves away from the vent. This model is currently restricted to compositions on the water-rich side of this chemical system and only predicts emplacement up to the turbulent to laminar transition. Modeling the laminar regime and a broader compositional space will be dealt with separately. Concentrations between 5 and 23 wt% (H_2O-NaCl eutectic) and initial flow thicknesses of 0.1, 1, 10, and 100 m were set as initial conditions. Model results suggest that flow may reach 40–60 vol% solids before transitioning to laminar flow. The thermal budget for these flows is dominated by the heat loss from vaporization in the low-pressure environment. This model produces length to thickness aspect ratios, for the given compositions, that are broadly consistent with candidate cryovolcanic features on Ceres and Titan. These first-order comparisons are not ideal and suggest the need for future modeling of cryovolcanic features in at least two dimensions.

Plain Language Summary Cryovolcanism is the icy volcanism that may occur on the surface icy bodies in the outer solar system. Erupted material will be predominantly aqueous fluid indicating that cryovolcanism lies at the intersection of volcanology and hydrology. However, neither discipline has models that adequately account for all of the parameters necessary for a cryovolcanic context. We produced a model for cryolava flow evolution that draws from both disciplines to track the physical, chemical, and thermal state of a hypothetical H_2O-NaCl flow. Results suggest that these flows may evolve more like a slush rather than a river with an expanding ice cap. These flows may also begin crystallizing while still in the turbulent regime. The transition to laminar flow may therefore be important to constrain, as it could be a point where a morphology or surface expression changes due to changing in behavior in the flow. Extending this model to different compositions and allowing more complicated mixtures may help to draw comparisons to observations of surface flows on icy satellites.

1. Introduction

The icy satellites and ocean worlds of the outer solar system display unique geologic features that may reflect processes analogous to those observed on the rocky bodies, but with a much different composition. Among these processes, cryovolcanism, the eruption of materials that would be volatile on Earth, but magma-like in far colder environments, has been invoked to explain a number of features. For example, resurfacing/smooth (at observational scale) terranes (Mitri et al., 2008; Showman et al., 2004), excess atmospheric volatiles (Choukroun et al., 2010; Quick et al., 2017; Tobie et al., 2006), plumes (Cooper et al., 2009; Manga & Wang, 2007; Roth et al., 2014; Sparks et al., 2017; Spencer et al., 2009), thermal anomalies (Abramov & Spencer, 2008, 2009), and/or surface constructs/flow features (Figueredo et al., 2002; Lopes et al., 2007; Ruesch et al., 2016) observed on many icy bodies. Many of these observed features show very similar morphologies to volcanic features found on Earth and the Moon (Figure 1), suggesting that similar processes may be involved in their formation.

Lava flow emplacement is well studied for silicate compositions (e.g., Costa & Macedonio, 2005; Dragoni, 1997; Harris & Rowland, 2001; Valerio et al., 2008; Williams et al., 2000). However, translating our knowledge of this process to cryogenic regimes in the outer solar system becomes complicated by factors that can generally be
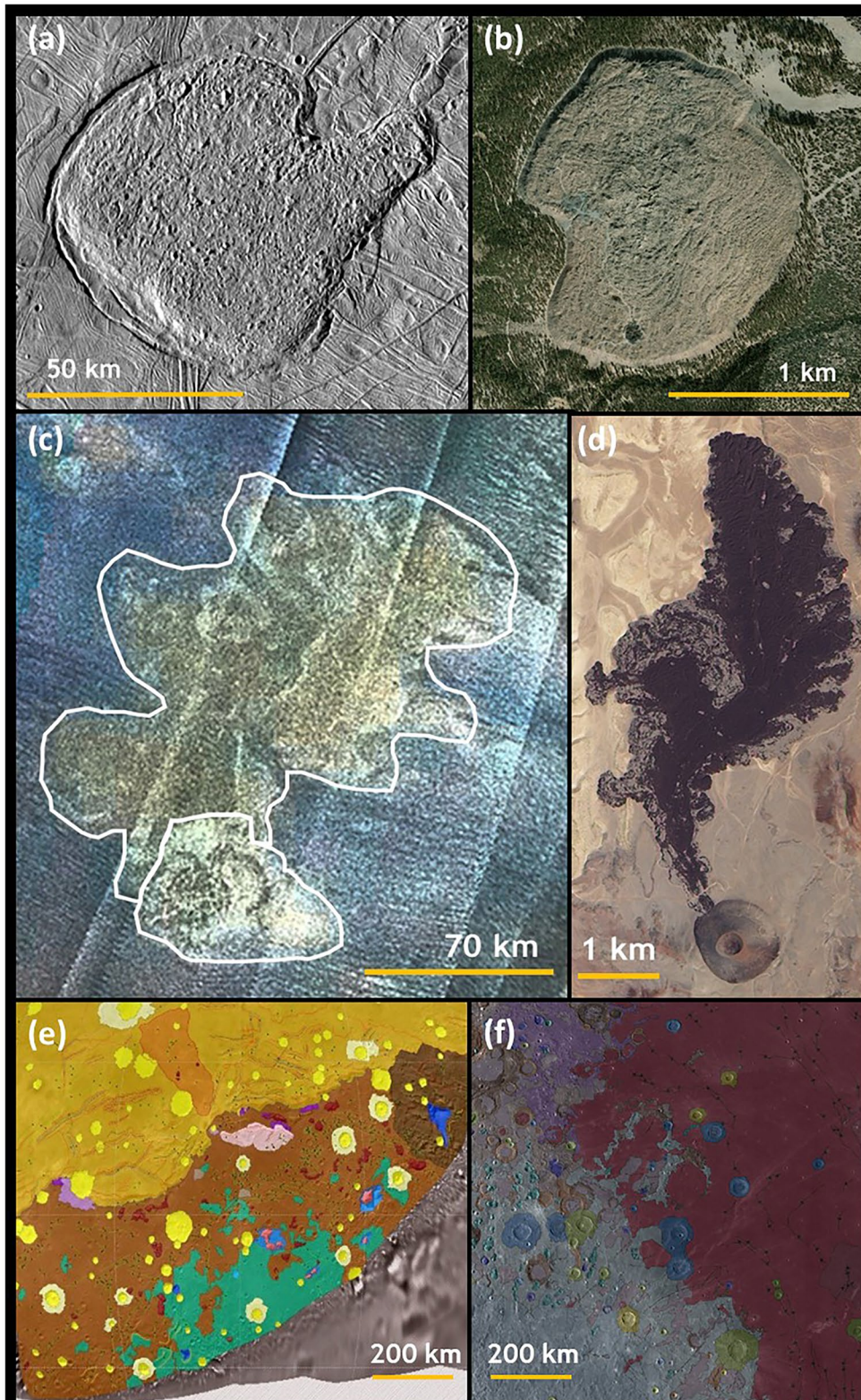
Figure 1.

neglected when studying silicate systems, such as vaporization or sublimation of lava. The cryovolcanic phenomenon is an interdisciplinary topic that lies at the intersection of volcanology and hydrology. By taking aspects of existing models from both disciplines, this study aims to present a new model for cryolava flow emplacement.

1.1. Physical Considerations of Water-Ice Flows

Cryovolcanism and effusive cryolava flows specifically occupy a unique position at the intersection of volcanology and hydrology. Cryolava flows are volcanic flows in the context of icy bodies but composed of very different materials to what is typically dealt with in the volcanology literature. Cryolava flows are dominated by water or brine, but exist in a very different context (pressure, temperature, gravity, etc.) than are typically dealt with in the hydrology literature.

As a dominantly water-rich composition erupts effusively into a low-pressure environment, the material (cryolava) will initially extend radially from a point source or laterally from a fissure, which typically reduces to one or more point sources over time (Wylie et al., 1999). Vaporization/boiling is likely the dominant mode of heat loss. Since the latent heat of vaporization for water is about seven times greater than that of fusion, the boiling off of a small amount of liquid will result in the formation of a much larger amount of ice. The material boils rapidly due to the low vapor pressure, quickly solidifying completely at the source if the effusion rate is relatively low. At higher effusion rates, flows may begin to channelize and extend further away from the vent.

Early carapace or roof formation is continuously disrupted by the turbulence, and vaporization of the underlying liquid water continues until the carapace becomes thick enough to exert sufficient hydrostatic/cryostatic pressure ($\sim$600 Pa) to counteract the vapor pressure and contain the flow, which is then insulated/isolated from the low-pressure environment. This thickness is about 0.5 m for Europa or Ganymede, assuming pure H_2O ice crystallization (Allison & Clifford, 1987; Quick et al., 2017). For higher (NaCl) brine content, the vapor pressure is lower (Dickson et al., 1965) and a smaller thickness is required. Quick et al. (2017) modeled dome emplacement on Europa and estimated that it would take $\sim$7.5 days for a 0.5 m carapace to form from a water-dominant composition and $\sim$2 days for a 0.25 m carapace to form from a 30% NaCl brine. These are much longer timescales than the several hours estimated by Allison and Clifford (1987) for flows on Ganymede, which has similar surface conditions to Europa, suggesting inconsistency in the literature with respect to timescales of potential cryolava flow evolution.

The relationship between carapace formation and flow turbulence has not been adequately considered in many previous works (see Section 1.2). This relationship has implications for how cryolavas evolve during emplacement. Specifically, many low-viscosity lavas on terrestrial bodies are tube-fed (Sauro et al., 2020), but the potential for tube formation as an emplacement mechanism depends on the ability of a lava flow to create a roof or crust. Tube formation in silicate lavas can result from surface cooling of a channelized flow (overcrusting), progressive growth from the margins of levees or shelves, or by inflation of existing lobes (Peterson et al., 1994). Cryolavas will have an additional complication of vaporization, as many of the icy bodies have little to no atmosphere. This vaporization will act to inhibit such overcrusting, and the turbulence of the low-viscosity flow would likely entrain the crystals that form as a result of vaporization-induced cooling. Therefore, we establish a working hypothesis of laminar flow being a prerequisite for the initiation of roof formation. If this is true, understanding where and when the turbulent to laminar transition occurs, and the physical state of the flow at that transition, becomes paramount to understanding cryolava flow emplacement.

We present a new model for the turbulent emplacement of cryovolcanic flows, combining elements from several previous models and addressing the shortcomings of each. The new model tracks the thermal evolution of the flow as well as its physical state until it reaches the turbulent to laminar transition. By doing so, we aim to predict the distances to which turbulent flows can extend, based on initial starting conditions, and determine the physical

Figure 1. Morphological comparison between volcanic flows and domes on Earth and icy bodies. (a) Murias Chaos, Europa ($\sim$100 $\times$ 77 km across, 235 m/pixel) imaged by Galileo SSI (image credit: NASA/JPL/University of Arizona). (b) Obsidian Dome, CA (1.3 $\times$ 1.8 km across, 50 cm/pixel) obtained from ESRI World Imagery (Maxar). (c) Doom Mons and Sotra Patera, Titan ($\sim$70 km edifice diameter, $\sim$180 km long flow, 175 m/pixel) imaged from Cassini SAR and VIMS (image credit: Lopes et al. (2013)). (d) SP Crater, AZ (1 km across, $\sim$7 km long flow, 50 cm/pixel) imaged by EO-1 ALI (image credit: NASA Earth Observatory, Jesse Allen & Robert Simmon). (e) Geologic map of the Vulcan Planitia region on Charon demonstrating large-scale flood-like features in the light brown (Beyer et al., 2019). Refer to Figure 2 of Beyer et al. (2019) for explanation of other colors. (f) Edge of Oceanus Procellarum in the Marius Hills region of the Moon, demonstrating the large flood-like Maria in the dark red. Image was produced using the Lunar Quickmap with the unified geologic map overlay (Fortezzo et al., 2020). Refer to sources for explanation of other colors.
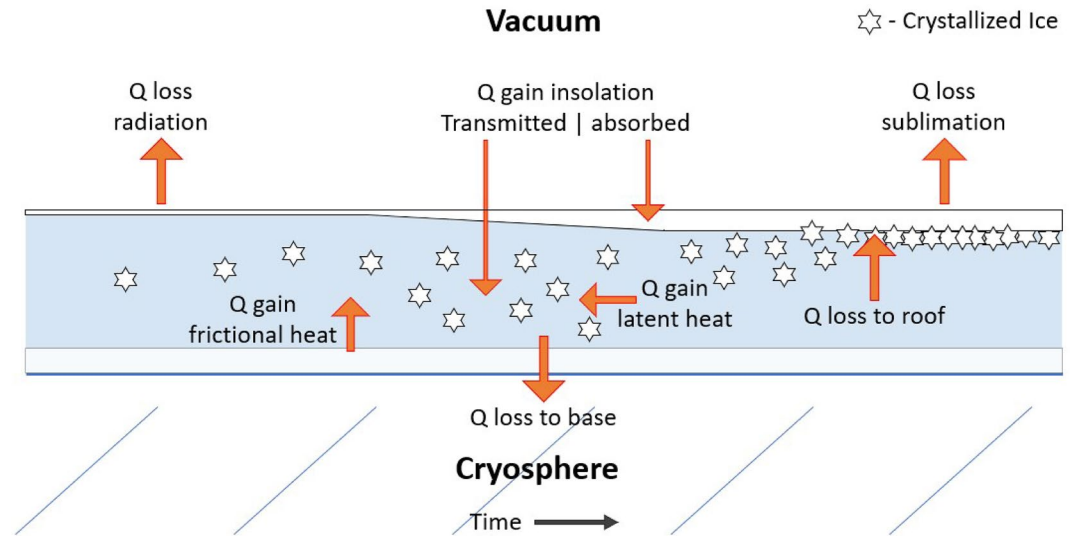
Figure 2. Schematic of evolution of hypothetical cryolava flow and the heat fluxes as defined by Allison and Clifford (1987). This conceptual model incorporated an ice covering from the initial emplacement that thickens over time.

state of the flow as it transitions to laminar behavior. This allows us to estimate aspect ratios (length:thickness) for turbulently emplaced cryolavas, in turn helping us to draw comparisons with morphologies of silicate flows, allowing further exploration of the silicate volcanism analogy. The working hypothesis of laminar flow being a prerequisite for roof formation is then revisited in light of the model results (see Section 5.4).

1.2. Previous Models

We draw on the literature/models from both volcanology and hydrology disciplines to model cryolava flow evolution. Williams et al. (2000) reevaluated the role of thermal erosion as a mechanism for lunar rille formation by modeling the heat budget and physical properties of a hypothetical lunar lava flow. This model is used throughout the planetary literature for examining channelized flows (Byrne et al., 2013; Hurwitz et al., 2012; Williams et al., 2001). The advantage of this model is the incorporation of a thermal erosion term that allows for downcutting into the substrate and assimilation of that material into the flow. However, the pitfalls of applying the Williams et al. (2000) model to cryovolcanism arise from the differences between silicate and aqueous systems. The heat budget for cryogenic systems is very different due to the low vapor pressures of the cryolavas and the rapid vaporization/crystallization that occurs when these liquids are exposed to the low-pressure surface environments of many icy bodies. The Williams et al. (2000) model also assumes a priori that the flow is incising a channel, that is, flow temperature is always above the melting point (solidus) of the substrate. For silicates, this assumption is valid since these values could be hundreds of degrees apart; the liquidus temperature of basalt is typically at least 200 K hotter than the solidus temperature. In the context of cryovolcanism, these temperatures are much closer (tens rather than hundreds of degrees apart, or even zero if pure water is considered), and this assumption becomes more tenuous. If the flow cools below the solidus temperature of the substrate (unlikely for silicates but expected for cryolavas), the thermal erosion term becomes negative and the equation breaks down. Even for silicate flows, it takes special conditions (long duration, high temperatures, and/or turbulence) to initiate thermal erosion.

Allison and Clifford (1987) modeled ice-covered water volcanism on Ganymede, using the thermal budget to assess flow evolution (i.e., thermal properties and ice cover thickness as a function of time) (Figure 2). This model is also heavily cited in the planetary literature when discussing extrusions of cryogenic material on icy bodies (Fagents, 2003; Kargel, 1991; Quick et al., 2017, 2019; Wilson et al., 1997). The advantage of this model is that it is already cryolava-specific, considers heat fluxes neglected in silicate systems (e.g., insolation), and incorporates crystallization of a roof or carapace. In practice, however, we believe that two of the simplifying assumptions may omit important characteristics of the cryolava flow evolution: (a) the flow is instantaneously emplaced and (b) a priori starts with an extremely thin ice crust that is allowed to thicken at each step. This is
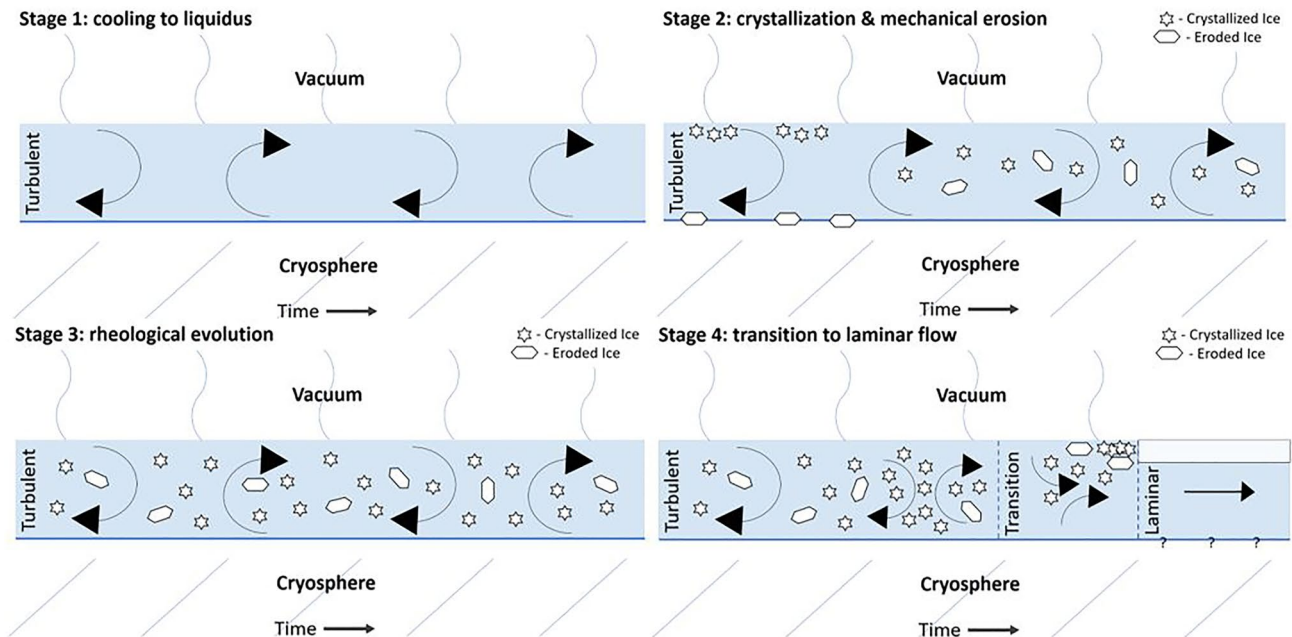
Figure 3. Conceptual model used in this work to define the expected behaviors during emplacement of a hypothetical turbulent cryolava flow. Each stage introduces new behaviors that have not previously been modeled together, tracking thermal, chemical, and physical changes simultaneously.

unreasonable due to the rapid boiling of the low vapor pressure material in the low-pressure environments that would disrupt initial formation of such a crust (Figure 2). Allison and Clifford (1987) admit that this assumption results in an underestimation of the early cooling rate, but suggest that the inaccuracy is outweighed by the benefit of reduction in complexity of the numerical model. Furthermore, the changing physical state of the flow (e.g., viscosity, Reynolds number, and crystal content) is not considered, making it difficult to track the physical properties at any given step in time or distance.

Bargery and Wilson (2011) modeled the erosive potential of large flooding events on Mars. The physics of flooding are fundamentally similar to that of an effusive cryolava flow. This hydrologic model provides a useful framework for a volcanic model in the context of an icy body. It takes into account the rapid boiling in a low-pressure environment, fluid dynamic evolution due to both crystallization and eroded substrate material (cf. xenoliths and stream load), and does not rely on the same assumption of a thickening crust during turbulent flow (Allison & Clifford, 1987). Instead, Bargery and Wilson (2011) modeled Martian flood events (i.e., water flows) in four stages: (a) cooling to the liquidus, (b) onset of crystallization, (c) transition to bedload sediment transport, and (d) transition to laminar flow. However, this model has only three heat fluxes: viscous heating, heat loss through evaporation, and heat loss to melt/warm eroded substrate (i.e., xenoliths, from the cryovolcanic perspective). They modeled cooling as only occurring from the surface, so that heat loss to the eroded substrate effectively contributes to surface cooling, and thermal gradients in/through the base/substrate can be ignored. This model is also only a physical model and chemical changes are not considered. This means that this model only applies to pure water flows and that cooling stops at 273 K. Our adaptation of this model to briny cryolava is further described in Section 2.

2. Model Overview

The model presented here will be divided into several stages (Figure 3) as delineated by Bargery and Wilson (2011). Stage 1 is initial emplacement where the cryolava is turbulent, crystal-free, and begins cooling to its liquidus (i.e., saturation temperature) by boiling in the low-pressure environment. If the flow temperature is above the melting temperature of the substrate, thermomechanical erosion may take place where energy would be lost to the (partial) melting and assimilation of icy substrate material. This process simultaneously downcuts and adds material to the flow (i.e., increases flow thickness). If the flow is not emplaced initially superheated, this stage will be bypassed and stage 2 will become the starting point. Stage 2 is the onset of crystallization as the flow
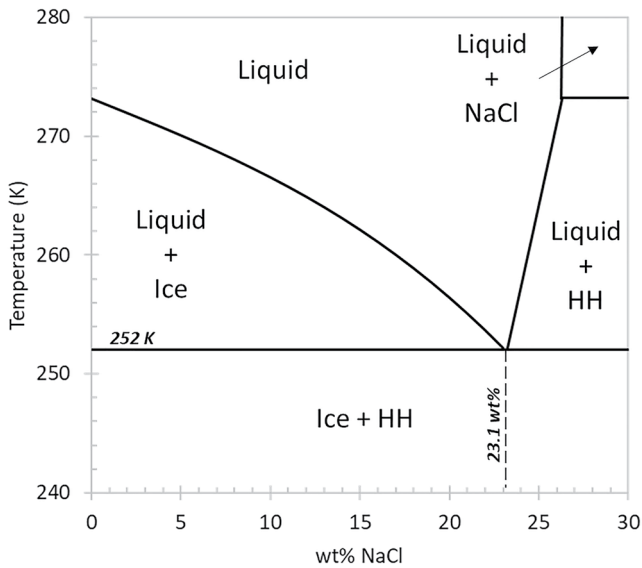
Figure 4. Dilute end of the H_2O-NaCl phase diagram used to define the liquidus, track crystallization (lever rule), and define the eutectic. Hydrohalite (NaCl•$2H_2O$) is abbreviated HH and curves were constructed from previous works (D. L. Hall et al., 1988; Sterner et al., 1988).

cools below the liquidus. The turbulence eliminates internal temperature gradients, allowing uniform cooling throughout the flow. The solid particles (crystals + eroded substrate fragments) are also entrained in suspension as long as turbulence persists and mean crystal diameter remains small. Entrained substrate ice is no longer melted but is warmed, adding to the total solid content and consequent bulk viscosity increase. Stage 3 begins when the increasing solid content of the flow markedly affects its rheology, that is, increasing viscosity and decreasing Reynolds number leading to the reduction of turbulence, and possible development of a yield strength. The heat lost via boiling/vaporization continues through this stage, a key difference from Bargery and Wilson (2011). This stage is analogous to rivers when washload (i.e., particle transport near the free surface) becomes bedload (i.e., particle transport near the base) (Bargery & Wilson, 2011). Stage 4 is the transition from turbulent to laminar flow that results from the increasing solid fraction. This final stage will be modeled separately and functionally represents the end of the model being presented here.

We assumed equilibrium crystallization, so that crystal fractions can be calculated from the phase diagram (Figure 4) for a given temperature and bulk composition. The substrate was assumed to be homogenous, crystalline water ice. Porosity, permeability, fracturing, and impurities or heterogeneities within this substrate were all factors that we exclude from this model that may be important in natural systems. Conduit behavior was also not considered here (e.g., pre-eruptive crystallization, volatile degassing, fragmentation, etc.). Although a gas phase may be expected in the conduit, and likely to escape at or near the vent, we did not include the effect of bubbles in the flow. We suggest that modeling a single-phase liquid with no bubbles can be considered a reasonable starting point.

We did not attempt to model complex multicomponent compositions, as much of the low-temperature thermodynamic data needed was not available for every relevant component (e.g., hydrates). Additionally, having multiple phases present exponentially increases the number of calculations and computation time for model execution. Therefore, we restricted this model to the water-rich side of simple binary aqueous systems to make implementation as straightforward as possible. Where compositionally specific data inputs were required, we used the H_2O-NaCl system as it has a well-characterized phase diagram, known low-temperature thermodynamic data, and may be an important non-water-ice component on Europa's surface and ocean (Hand & Carlson, 2015; Poston et al., 2017).

3. Model Formulation

3.1. System Definitions and Initial Conditions

This model required definition of several chemical and physical parameters to be known and explicitly defined. These included: starting temperature of the erupted material (T_0), ambient surface temperature (T_a), substrate melting temperature (T_{sub}), eutectic temperature of the chemical system chosen (T_{eu}), eutectic composition for the chemical system chosen (X_{eu}), starting composition of the initial liquid (X_0), substrate density (ρ_{sub}), density of the crystallizing ice (ρ_{ice}), density of the eutectic crystallizing phase (ρ_{salt}), diameter of crystallizing particles (D), initial flow thickness (h_0), ambient surface pressure (P_a, can often be set to zero for negligible atmospheres), local ground slope (α), and gravity (g). These values were all considered constants within each model run.

In setting up the model, we assumed that cryolavas would be aqueous brines restricted to simple binary solutions on the water-rich side of the eutectic. We specifically used the H_2O-NaCl system to demonstrate this model as it represents relevant constituents for extrusions on Europa with all of the required data being readily available. Real cryolavas will be more complex multicomponent brine mixtures, in part, dependent on the formation mechanism (e.g., Fagents et al., 2022; Melwani Daswani et al., 2021). We defined the starting temperature for the model as 273 K as that is the likely temperature of the ocean at the base of Europa's ice shell (Melosh et al., 2004). Sub-ambient thermal properties (e.g., heat capacity, latent heat, vapor pressure, etc.) were not available in some

Table 1
Coefficients for Liquid Density (Equation 8) From Sharqawy et al. (2010)

$b_1 = 999.9$	$b_6 = 802.0$
$b_2 = 2.034 \times 10^{-2}$	$b_7 = -2.001$
$b_3 = -6.162 \times 10^{-3}$	$b_8 = 1.677 \times 10^{-2}$
$b_4 = 2.261 \times 10^{-5}$	$b_9 = -3.060 \times 10^{-5}$
$b_5 = -4.657 \times 10^{-8}$	$b_{10} = -1.613 \times 10^{-5}$

other binary chemical systems. The model functions by calculating the material properties and thermal budget at each time step to track flow behavior as it changes in temperature and crystal content. The Reynolds number was used to track the flow regime (i.e., turbulent or laminar) at each time increment of the model, and the model ends once the laminar flow regime was reached. However, flow velocity (u), friction factor (f), and Reynolds number (Re) are interdependent values, and therefore, were iteratively solved using the following equations (Williams et al., 2000):

$$u_{\text{turb}} = \sqrt{\frac{4gh \sin \alpha}{f}} \tag{1}$$

$$f = [0.79 \ln(\text{Re}) - 1.64]^{-2} \tag{2}$$

$$\text{Re}_{\text{turb}} = \frac{4\rho_{\text{bulk}} h u_{\text{turb}}}{\eta_{\text{bulk}}}. \tag{3}$$

The surface gravity of the body is g (m s^{-2}), the flow thickness is h (m), and the ground slope is α, taken to be 0.1°, ρ_{bulk} is the bulk flow density (kg m^{-3}), and η_{bulk} is the bulk flow viscosity (Pa s). Equation 1 was modified from Britter and Linden (1980) and Jarvis (1995) and represents the velocity in response to gravity with no mass flux imposed. Equation 2 is the friction factor for pipe flow from Kakaç et al. (1987). Equation 3 is the general form of the Reynolds number equation, which assumes that the characteristic length is the flow thickness (see Appendix A). The iteration of these equations was done at each time step. Additionally, we calculated the laminar velocity and laminar Reynolds number,

$$u_{\text{lam}} = \frac{\rho_{\text{bulk}} gh^2 \sin \alpha}{3\eta_{\text{bulk}}} \tag{4}$$

$$\text{Re}_{\text{lam}} = \frac{4\rho_{\text{bulk}} h u_{\text{lam}}}{\eta_{\text{bulk}}}. \tag{5}$$

The critical Reynolds number represents the transition between turbulent and laminar regimes. Since the flow constantly evolves with temperature-dependent properties, the critical Re value will also be a moving target. Thus, instead of using a defined critical value that is valid for a single state of an evolving flow, the turbulent to laminar transition was determined by when the laminar Reynolds number became less than or equal to the turbulent Reynolds number. Knowing the flow velocity (Equation 1) and defining the time step of the model (Δt) allow the distance away from the vent to be simply determined by

$$ = d_{t-1} + u_{\text{turb}} \Delta t. \tag{6}$$

where d_{t-1} is the distance (or flow length) from the previous time step, where $d = 0$ at $t = 0$.

The density used in these equations was the bulk density of the flow (ρ_{bulk}), which we calculated as a function of both temperature and concentration using the following equation:

$$\rho_{\text{bulk}} = (1 - \varphi_{\text{ice}} - \varphi_{\text{salt}}) \rho_{\text{liq}} + \varphi_{\text{ice}} \rho_{\text{ice}} + \varphi_{\text{salt}} \rho_{\text{salt}} \tag{7}$$

where φ_{ice} is the weight fraction of crystallized ice (Section 3.2), φ_{salt} is the weight fraction of crystallized salt, which only occurs at the eutectic, ρ_{liq} is the density of the liquid phase, ρ_{ice} is the density of crystallizing ice (920 kg m^{-3}), and ρ_{salt} is the density of the eutectic crystallizing salt phase (hydrohalite: 1,610 kg m^{-3}). The temperature-dependent liquid density was taken from Equation 8 of Sharqawy et al. (2010):

$$\rho_{\text{liq}} = \sum_{n=1}^{5} b_n (T - 273.15)^{n-1} + \sum_{n=6}^{9} b_n X (T - 273.15)^{n-1} + b_{10} X^2 (T - 273.15)^2 \tag{8}$$

where b_n coefficients are provided in Table 1.

The following sections explain how the model handled various parameters. Section 3.2 focuses on the liquidus and crystallization calculations, Section 3.3 discusses how the model incorporated the erosion rate, Section 3.4

explains how the rheological evolution of the flow was tracked, Section 3.5 defines the thermal budget and temperature evolution, and Section 3.6 explains how model calculations were updated once the eutectic was reached.

3.2. Liquidus and Crystal Fraction

Crystallization was a key component of the model as it affects both the heat budget (latent heat of fusion) and the rheology (viscosity and Reynolds number). In order to know when crystallization begins, an accurate liquidus temperature (cf. saturation temperature and solubility curve) was required. For simple chemical systems, like the H_2O-NaCl system, the liquidus can be determined as a function of temperature and composition from the phase diagram and equations of state. For the H_2O-NaCl system, these are very well defined equations. D. L. Hall et al. (1988) presented the following equations of freezing point depression (i.e., liquidus, T_{liq}) for the H_2O-NaCl-KCl system:

$$T_{liq} = 273.15 - \left[C_1(100X_0) + C_2(100X_0)^3 \right] \tag{9}$$

$$C_1 = 0.4597 + 0.1440S \tag{10}$$

$$C_2 = 2.227 \times 10^{-4} + 1.999 \times 10^{-4}S + 4.633 \times 10^{-5}S^2 + 1.123 \times 10^{-4}S^3 \tag{11}$$

where T_{liq} is in K, X_0 is the weight fraction of the NaCl in the initial liquid (i.e., salinity), and C_1 and C_2 are experimentally determined coefficients where S is the NaCl/(NaCl + KCl) ratio. Here, we considered only the H_2O-NaCl system, so that S remains constant at unity, and C_1 and C_2 become constants of 0.6037 and 5.8123×10^{-4}, respectively.

Knowing the starting composition, the crystal fraction of ice was then calculated for any given temperature between the liquidus and eutectic (T_{eu}) using the lever rule. Bodnar (1993) rearranged the equation from D. L. Hall et al. (1988) and put it in terms of temperature rather than composition

$$X(T) = 1.78 \times 10^{-2}(273.15T) - 4.42 \times 10^{-4}(273.15 - T)^2 + 5.57 \times 10^{-6}(273.15 - T)^3 \tag{12}$$

where X is the weight fraction of NaCl in the bulk liquid as the flow evolves toward the eutectic. Applying the lever rule functionally results in the following equation:

$$\varphi_{ice} = \frac{X(T) - X_0}{X(T)} = \frac{\left(1.78(273.15 - T) - 0.0442(273.15 - T)^2 + 5.57 \times 10^{-4}(273.15 - T)^3\right) - 100X_0}{\left(1.78(273.15 - T) - 0.0442(273.15 - T)^2 + 5.57 \times 10^{-4}(273.15 - T)^3\right)}. \tag{13}$$

For the rest of the model, it was more useful to track X as a function of φ_{ice}, so we redefine X as follows:

$$(\varphi_{ice}) = \frac{X_0}{1 - \varphi_{ice}}. \tag{14}$$

The above equations (Equations 9–14) are only valid between the liquidus and eutectic temperatures. Once the eutectic is reached, X was buffered at the eutectic composition (X_{eu}), and an additional solid phase (φ_{salt}) begins co-crystallizing. The rate at which crystallization proceeds at the eutectic will be discussed in Section 3.6.

The crystal weight fractions (φ) can be converted to volume fractions (ϕ) by the following:

$$V_{tot} = \frac{\varphi_{ice}}{\rho_{ice}} + \frac{\varphi_{salt}}{\rho_{salt}} + \frac{1 - \varphi_{ice} - \varphi_{salt}}{\rho_{liq}} \tag{15}$$

$$\phi_{ice} = \frac{\varphi_{ice}}{\rho_{ice}V_{tot}} \tag{16}$$

$$\phi_{salt} = \frac{\varphi_{salt}}{\rho_{salt}V_{tot}}. \tag{17}$$

The total amount of crystallized solids in the flow was then:

$$\Sigma\varphi_{xtal} = \varphi_{ice} + \varphi_{salt} \tag{18}$$

or

$$\Sigma\phi_{xtal} = \phi_{ice} + \phi_{salt} \qquad (19)$$

for weight fraction or volume fraction, respectively.

3.3. Erosion/Incision Rate

Erosion (incision) rates of the substrate (bed) were important to consider as it may play a role in flow evolution in multiple ways. Substrate erosion can occur by mechanical erosion, thermal erosion, and/or thermomechanical erosion. Mechanical erosion occurs by the physical removal of substrate material via plucking, abrasion, and/or cavitation (Whipple et al., 2000). We incorporated a solid fraction of substrate, assumed pure water ice, which was mechanically eroded from the base of the flow (cf. xenoliths), which was included in the ice fraction:

$$\phi_{erod} = \frac{h_{er}}{h}. \qquad (20)$$

where h_{er} is the thickness (or depth) of material eroded from the substrate. This equation provides the instantaneous volume fraction of substrate material added to the flow for any given time step. Thus, we also calculated the cumulative volume fraction of eroded material added to the flow as

$$\Sigma\phi_{erod} = \sum_{t=0}^{t} \phi_{erod,t}. \qquad (21)$$

The depth of material eroded (h_{er}) was calculated by

$$h_{er} = E_{mech}\Delta t \qquad (22)$$

where E_{mech} is the mechanical erosion rate (m s^{-1}). We note that the particle size distribution of the eroded material was not strictly defined and unlikely to be the same as the suspended, crystallized particles. However, to simplify the calculations, we assumed that the eroded material was equivalent to the crystallized material in size in order to neglect thermal and/or rheological heterogeneities in the flow.

Many of the equations and relations for mechanical erosion rates used in previous studies tend to be based on observational, empirical, or dimensional parameters that are not easily obtained (Hurwitz et al., 2010, 2012; Sklar & Dietrich, 1998, 2001; Whipple, 2004; Whipple et al., 2000). Generally accepted relationships for how volume fraction concentration or flow dynamics control mechanical erosion rate does not exist (Bargery & Wilson, 2011). We thus treated the mechanical erosion rate as follows:

$$E_{mech} = \left(\frac{e}{Y}\right) hu\rho_{bulk} g \sin\alpha \qquad (23)$$

where e is the erodibility of the substrate and Y is the strength of the substrate (Hurwitz et al., 2010). The ratio of erodibility to strength of the substrate represents the efficiency of incision (Sklar & Dietrich, 1998). This ratio also "aggregates the influence of many factors, including channel geometry, hydraulic roughness, the magnitude-frequency relations implicit in the assumption of a dominant discharge, and rock resistance to erosion, which will vary with incision process, rock type, degree of weathering and tectonic history" (Sklar & Dietrich, 1998). Functionally, this means that the values for both e and Y are very sensitive to the geologic context and thus poorly constrained for compositions and conditions at the surface of icy bodies. Therefore, we opted to use the values in Table 1 of Hurwitz et al. (2010) for erodibility and strength of the substrate. These parameters were intended for incision of basaltic lava into basaltic substrate on Mars. We would expect the erodibility to be higher and strength to be lower for ices than silicates, however, by exactly how much is uncertain. Without this information, we maintained the basaltic values as an approximation.

Thermal erosion will only occur when the flow temperature is above the melting point (solidus) of the substrate. As potential cryolavas are only likely to be superheated by a few degrees at most, if at all (Melosh et al., 2004), thermal erosion is only expected to be possible very near to the vent. Therefore, we did not include thermal erosion in this model. Thermomechanical erosion is a combination of thermal and mechanical erosion where the substrate is partially melted, allowing for more efficient mechanical erosion. Since we assume that thermal erosion is not important in the cryovolcanic context, and that the substrate is pure water ice instead of an impure

mixture, thermomechanical erosion was also neglected. Hence, only mechanical erosion was taken into account here.

3.4. Rheology

Many models exist for suspension rheology, that is, viscosity evolution as a function of solid volume fraction (Costa et al., 2009; Krieger & Dougherty, 1959; Roscoe, 1952, etc.). The choice of model becomes very important for suspensions at moderate- to high-volume fractions, because changes in viscosity are many orders of magnitude from vent to final emplacement. Costa et al. (2009) produced a model for fitting bulk viscosity data of suspensions as a function of volume fraction. When plotted on a graph of log viscosity against volume fraction, this equation has a sigmoidal form. This represents the evolution of a crystallizing material better than other commonly used models, which asymptotically approach infinite viscosity at a critical solid volume fraction much less than 1, often close to the maximum packing fraction (Mader et al., 2013). At small-volume fractions, bulk viscosity is low, and the material is dominated by liquid behavior, so small amounts of solids do not influence the bulk material behavior much. At large volume fractions, the viscosity is high and the material is dominated by solid behavior, so small amounts of liquid do not influence the bulk material behavior much. However, at intermediate volume fractions, the bulk viscosity evolves rapidly from liquid-like to solid-like behavior.

These behaviors can all be captured by an equation with the following form (Costa et al., 2009):

$$\eta_r = \frac{1 + \left(\frac{\phi_{\text{total}}}{\phi^*}\right)^\delta}{(1 - C_3)^{B\phi^*}} \tag{24}$$

where

$$C_3 = (1 - \xi)\text{erf}\left[\frac{\sqrt{\pi}}{2(1 - \xi)}\frac{\phi_{\text{total}}}{\phi^*}\left(1 + \left(\frac{\phi_{\text{total}}}{\phi^*}\right)^\gamma\right)\right] \tag{25}$$

$$\phi_{\text{total}} = \Sigma\phi_{\text{xtal}} + \Sigma\phi_{\text{erod}}. \tag{26}$$

where η_r is the relative viscosity, which is the ratio of bulk or apparent viscosity to the viscosity of the liquid phase ($\eta_r = \eta_{\text{bulk}}/\eta_{\text{liq}}$). This convention allows for the comparison of the physical effect on viscosity imparted by the total solid volume fraction (ϕ_{total}) across different materials/compositions. ϕ^* is the critical volume fraction at the onset of the rapid increase in viscosity (not the maximum packing fraction); δ, γ, and ξ ($<<1$) are empirical fitting parameters; and B is the Einstein coefficient with a nominal value of 2.5 for uniform spheres. The value of B depends on shape and size distribution of particles but has analytical solutions for only limited, simple cases (Brenner, 1974; Haber & Brenner, 1984; Rallison, 1978; Wakiya, 1971). Additionally, γ is a measure of how rapidly the relative viscosity increases as ϕ_{total} approaches ϕ^*, while δ controls how fast relative viscosity increases as ϕ_{total} becomes greater than ϕ^*.

For the viscosity of brine (η_{liq}), we used Equation 22 of Sharqawy et al. (2010):

$$\eta_{\text{liq}} = \eta_w\left(1 + C_4X + C_5X^2\right) \tag{27}$$

$$C_4 = 1.541 + 1.998 \times 10^{-2}T - 9.52 \times 10^{-5}T^2 \tag{28}$$

$$C_5 = 7.974 - 7.561 \times 10^{-2}T + 4.724 \times 10^{-4}T^2 \tag{29}$$

where η_w is the viscosity of pure water and C_4 and C_5 are temperature-dependent polynomials. The equation for water viscosity comes from the IAPWS 2008 (International Association for the Properties of Water and Steam, 2008):

$$\eta_w = 4.2844 \times 10^{-5} + \left(0.157(T + 64.993)^2 - 91.296\right)^{-1}. \tag{30}$$

We recognize that using the relation of Costa et al. (2009) as a predictive model for bulk viscosity imparts some uncertainty to our results and requires some assumptions to be made. Because of the lack of experimental studies relating B to particle aspect ratio and orientation, especially for crystallizing ice, we used the value for uniform
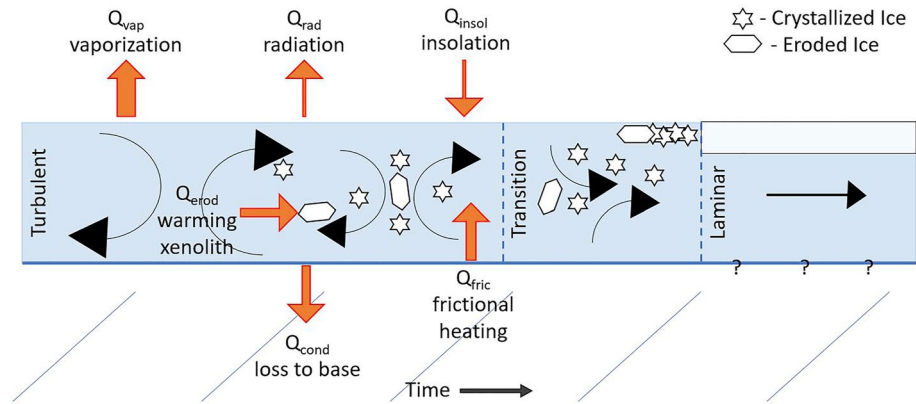
Figure 5. Heat fluxes considered for modeling the turbulent regime of a hypothetical cryolava extrusion. Orange arrow size represents the qualitative relative magnitude of each heat flux.

spheres. To remain consistent, we also use values for uniform spheres for the other empirical fitting parameters δ, γ, and ξ (Mader et al., 2013).

The apparent yield strength of the flow was also tracked during crystallization. We used Equation 30 of Bargery and Wilson (2011) to calculate yield strength (σ_y),

$$\sigma_y = 0.1341 e^{10.14 \phi_{total}}. \tag{31}$$

This equation is an empirical fit to the data of Huang and García (1998), Parsons et al. (2001), and Bowles et al. (2003). While empirical, it allows for yield strength calculations for turbulent flow up to the high solid fraction. We additionally note a likely typographical error in the original text, which has the solid fraction term outside of the exponential. We recognize that it may be counterintuitive to track a yield strength in a model of turbulent flow. However, this apparent yield strength may be an important term in rheological laws for suspensions and may become an important term for understanding flow cessation (see Section 5).

3.5. Thermal Budget

The model functions by calculating the material properties for a given composition at a given temperature and then calculating the heat balance to determine the change in temperature for the next time step. Figure 5 depicts the different heat fluxes considered in this model. The thermal budget was defined by the following:

$$\Delta Q = \Sigma Q_{gain} - \Sigma Q_{loss} = [Q_{insol} + Q_{fric}] - [Q_{vap} + Q_{erod} + Q_{cond} + Q_{rad}] \tag{32}$$

where the change in thermal energy (ΔQ) is the difference between the sum of the heat gain terms and the sum of heat loss terms. Each of the constituent terms will be discussed in detail further. Additionally, the treatment of latent heat will be described in Equations 54 and 55.

Heat gained by insolation (Q_{insol}) is a heat flux that is typically ignored in lava flow modeling. Due to the much lower surface temperatures of outer solar system bodies, we have included it here. We used the equation of Allison and Clifford (1987),

$$Q_{insol} = I(1 - A), \tag{33}$$

where I is the incident insolation and A is the mean albedo. The value for I used here was 50.04 W m^{-2}, which is the solar constant for the Jupiter system (Allison & Clifford, 1987). Using this value ensures that the insolation heat flux was the maximum possible for all calculations. The other heat gain term is frictional heat (Q_{fric}), which is generated by converting head loss directly to heat. The equation of Allison and Clifford (1987) was used as follows:

$$Q_{fric} = u_{turb} \rho_{bulk} h g \sin \alpha. \tag{34}$$

The justification for the implicit assumptions of both of these heat gain terms will be further discussed in Section 5.2.

The heat loss terms dominate the system, resulting in net cooling of the flow. Heat flux from radiative cooling was simple to implement, as it is strictly temperature and emissivity dependent. Radiative cooling (Q_{rad}) was calculated as

$$Q_{rad} = \sigma \varepsilon T^4 \tag{35}$$

where σ is the Stefan-Boltzmann constant and ε is the emissivity, assumed to be 0.98 (Hori et al., 2006).

Heat loss through the base of cryolava flows has previously been implemented in three different ways. Allison and Clifford (1987) used a finite difference method to determine the heat flux at the base of the flow. Williams et al. (2000) calculated the heat loss at the base of the flow from the product of a convective heat transfer coefficient (Huppert & Sparks, 1985; Williams et al., 2000) and the temperature difference between the flow and substrate melting temperature. Bargery and Wilson (2011) did not calculate a basal heat loss term directly, but argued that the eroded substrate material is continually incorporated into the flow, so that cooling results from heat transfer to the eroded material (xenoliths) rather than to the substrate. Of these three treatments, the finite difference method (Allison & Clifford, 1987) is the most rigorous, but can be time consuming and dramatically increases computing time when many iterations are required.

As a compromise, we elected to model the heat flux through the base of the flow (Q_{cond}) as follows:

$$Q_{cond} = k\left(T_{avg}\right)\left[\frac{T_{avg}}{z}\right] \tag{36}$$

where $k(T_{avg})$ is the thermal conductivity of water ice at the average temperature between the flow (T) and the substrate (T_a) over a depth (z) within the substrate (we considered the top 0.2 m of the substrate). The exact depth chosen will be shown to be inconsequential in Section 5.1. This equation models the heat flux without the thermal wave propagating through the substrate (i.e., the substrate is always at the fixed ambient surface temperature). This also means that Q_{cond} is always overestimated except for when the flow makes initial contact (see Section 5.1). The equation for thermal conductivity of ice comes from Ratcliffe (1962).

$$k_{ice} = 12.52 - 6.092 \times 10^{-2}T + 1.15 \times 10^{-4}T^2. \tag{37}$$

Because we included mechanical erosion, we also considered the heat lost to warming the eroded substrate material (Q_{erod}). Our equation was modified from Equation 23 of Bargery and Wilson (2011):

$$Q_{erod} = \begin{cases} \rho_{ice}h_{er}c_{ice}\left(T_{sub} - T_a\right) + \rho_{ice}h_{er}L_f^{ice} + \rho_w h_{melt}c_w\left(T - T_{sub}\right), & T > T_{sub} \\ \rho_{ice}h_{er}c_{ice}\left(T - T_a\right), & T < T_{sub} \end{cases}, \tag{38}$$

where c_{ice} is the specific heat of ice (substrate), T_{sub} is the melting temperature of the substrate material, L_f^{ice} is the latent heat of fusion of ice, h_{melt} is the thickness of eroded (and melted) substrate material adjusted for the volume difference between ice and water, and c_w is the specific heat of water. When flow temperature is greater than the melting point of the substrate, energy is required to warm the eroded substrate material from the ambient surface temperature to its melting temperature, for the phase change itself, and then to warm the melted material to the flow temperature. However, if the flow temperature is below the melting point of the substrate, energy only goes into warming the eroded substrate material from the ambient surface temperature to the flow temperature.

The specific heat of ice (c_{ice}) was taken from Equation 16 of Ellsworth and Schubert (1983):

$$c_{ice} = 7.037T + 185. \tag{39}$$

We note that there is a typographical error in this paper where the units for this value were described as kJ kg^{-1} K^{-1} but are actually J kg^{-1} K^{-1}. At the eutectic, a second phase will co-crystallize. For the H_2O-NaCl system, that phase is hydrohalite (NaCl•$2H_2O$) with specific heat adapted from Equation 9 of Drebushchak and Ogienko (2020).

$$c_{\text{salt}} = \left(8 \times 10^{-5}T^2 - 0.0285T + 5.0365\right) c_{\text{NaCl}} - 0.248 c_{\text{ice}} \tag{40}$$

where c_{NaCl} is the specific heat of pure NaCl in J kg^{-1} K^{-1}. The polynomial term is a quadratic fit to their measured data in their Table 2. The following equation for specific heat of NaCl was fit to the data in Table 5 of Archer (1997) using a cubic polynomial and divided through by the molar mass of NaCl for unit consistency:

$$c_{\text{NaCl}} = 2 \times 10^{-8}T^3 - 2 \times 10^{-5}T^2 - 6.3 \times 10^{-3}T + 0.1476. \tag{41}$$

The equation used for the liquid/brine phase (c_{liq}) was taken from Equation 19 of Millero et al. (1973):

$$c_{\text{liq}} = c_{\text{w}} + C_6(1000X) + C_7(1000X)^{1.5} \tag{42}$$

$$C_6 = -13.81 + 0.1938(T - 273.15) - 0.0025(T - 273.15)^2 \tag{43}$$

$$C_7 = 0.43 - 0.0099(T - 273.15) + 0.00013(T - 273.15)^2 \tag{44}$$

where c_{w} is the specific heat of pure water, also taken from Millero et al. (1973):

$$c_{\text{w}} = 4217.4 - 3.72(T - 273.15) + 0.141(T - 273.15)^2 - 2.654$$
$$\times 10^{-3}(T - 273.15)^3 + 2.093 \times 10^{-5}(T - 273.15)^4, \tag{45}$$

and C_6 and C_7 are temperature-dependent polynomials. We used these specific heat equations for brine and water over more recent equations due to their ability to reasonably extrapolate down to lower temperatures beyond the range of calibration of the original equations, which were 278 and 308 K and 0 to 2.2 wt% NaCl (Millero et al., 1973). The heat capacity for the bulk flow was then calculated from the weight fractions of solid and liquid constituents by

$$c_{\text{bulk}} = \left(1 - \varphi_{\text{ice}} - \varphi_{\text{salt}}\right) c_{\text{liq}} + \varphi_{\text{ice}} c_{\text{ice}} + \varphi_{\text{salt}} c_{\text{salt}}. \tag{46}$$

The final heat flux considered was the vaporization of the liquid material in the low-pressure environment. The heat loss from vaporization (Q_{vap}) was calculated following Equation 22 of Bargery and Wilson (2011):

$$Q_{\text{vap}} = L_{\text{v}} \frac{dm}{dt}, \tag{47}$$

where L_{v} is the latent heat of vaporization for the liquid phase, and dm/dt is the mass loss rate of material in kg m^{-2} s^{-1}. Bargery and Wilson (2011) stated that the latent heat of vaporization has a slight temperature dependence,

$$L_{\text{v}} = 2.5 \times 10^6 - 2730.1T, \tag{48}$$

which we have included. The mass loss rate was calculated from the equation of Kennard (1938):

$$\frac{dm}{dt} = Z\left(P_{\text{liq}} - P_{\text{a}}\right)\left(\frac{M_{\text{w}}}{2\pi RT}\right)^{0.5} \tag{49}$$

where Z is the coefficient of evaporation, empirically determined to be 0.94 for water or ice (Tschudin, 1946), P_{liq} is the vapor pressure of the liquid in the flow, P_{a} is the ambient surface pressure (which can be neglected for most icy bodies), M_{w} is the molecular weight of the vaporizing phase (in this case water), and R is the universal gas constant. Vapor pressure (in Pa) as a function of temperature and concentration was taken from Equation 5 of Nayar et al. (2016).

$$P_{\text{liq}} = P_{\text{H2O}} \times \text{EXP}\left(-4.58180 \times 10^{-4}(1000X) - 2.04430 \times 10^{-6}(1000X)^2\right) \tag{50}$$

where vapor pressure of pure water is:

$$P_{\text{H2O}} = 133.3\text{EXP}\left(\frac{-5631.1206}{T} + 18.95304\log_{10}T - 0.03861574T + 2.77494 \times 10^{-5}T^2 - 15.55896\right) \tag{51}$$

(Allison & Clifford, 1987; Clifford & Hillel, 1983; Lebofsky, 1975; Washburn et al., 1926). The mass loss rate of material was converted to a change in thickness by the following:

$$h_v = E_v \Delta t = \frac{1}{\rho_{\text{bulk}}} \frac{dm}{dt} \tag{52}$$

where E_v is a vaporization rate in m s^{-1}.

The value for flow thickness for any given time step was then determined as follows:

$$h = h_{t-1} + h_{\text{er},t-1} - h_{v,t-1} = h_{t-1} + E_{\text{mech},t-1}\Delta t - E_{v,t-1}\Delta t, \ h = h_0 \text{ at } t = 0 \tag{53}$$

where the thickness from the previous time step gains the amount eroded from the substrate during the previous time step and loses the amount vaporized during the previous time step.

With each different flux defined, we then calculated the change in temperature of the flow for the upcoming time step by

$$\Delta T = \frac{\Delta Q \Delta t}{\rho_{\text{bulk}} h \left(c_{\text{bulk}} + \varphi_{\text{ice}} L_f^{\text{ice}} \right)} \tag{54}$$

This equation allows the change in internal energy of the flow to be partitioned into sensible and latent heat components. Thus, the latent heat is included implicitly in this model rather than explicitly (e.g., Allison & Clifford, 1987). Equation 54 is the key term solved at each step to define the starting temperature for the following step.

3.6. Eutectic Crystallization

Once the eutectic was reached, the temperature of the system was buffered until it completely crystallized or the model ended. Additionally, the eutectic introduced a second crystallizing phase, in this case hydrohalite, which needed to be accounted for in the crystal/solid fraction. Therefore, we calculated how much total crystallization was occurring at each time step, which was then partitioned into the two different crystallizing phases. To accomplish this, we used the following equation:

$$\Delta \varphi_{\text{total}} = \frac{\Delta Q}{\rho_{\text{bulk}} h \left((1 - X_{\text{eu}}) L_f^{\text{ice}} + X_{\text{eu}} L_f^{\text{salt}} \right)} = \frac{\Delta Q}{\rho_{\text{bulk}} h L_f^{\text{eutectic}}} \tag{55}$$

where $\Delta \varphi_{\text{total}}$ is the total amount of additional crystal fraction added (in weight fraction) at the given time step, ΔQ is the heat flux (W m^{-2}), ρ_{bulk} is the bulk density of the flow (in kg m^{-3}), X_{eu} is the eutectic composition (in weight fraction), and L_f is the latent heat of fusion for ice and hydrohalite, respectively (in J kg^{-1}). We note here that the latent heat of fusion and other thermodynamic properties of hydrohalite are difficult to determine experimentally due to difficulties crystallizing large quantities. Latent heats of fusion were measured by Drebushchak and Ogienko (2020) for hydrohalite, and by Han et al. (2006) for H$_2$O-NaCl eutectic solution crystallization. Because of these difficulties and the fact that the eutectic composition (typically in terms of anhydrous solute) must be adjusted when considered in terms of a hydrated mineral, we have made a substitution in Equation 55 for the latent heat of the eutectic solution (L_f^{eutectic}) from Han et al. (2006), rather than trying to adjust eutectic compositions. Once the change in total crystal fraction was determined, it was partitioned between ice and hydrohalite by the ratio of H$_2$O to NaCl at the eutectic as follows:

$$\varphi_{\text{ice}} = \varphi_{\text{ice},t-1} + (1 - X_{\text{eu}}) \Delta \varphi_{\text{total},t-1} \tag{56}$$

$$\varphi_{\text{salt}} = \varphi_{\text{salt},t-1} + X_{\text{eu}} \Delta \varphi_{\text{total},t-1} \tag{57}$$

where the change in total crystal content partitioned by the phase from the previous time step is added to the crystal content of the previous time step. Due to the complexity of all the interdependent parameters, a flowchart of operations has been created to help visualize how this process was carried out at each time step (Figure 6).
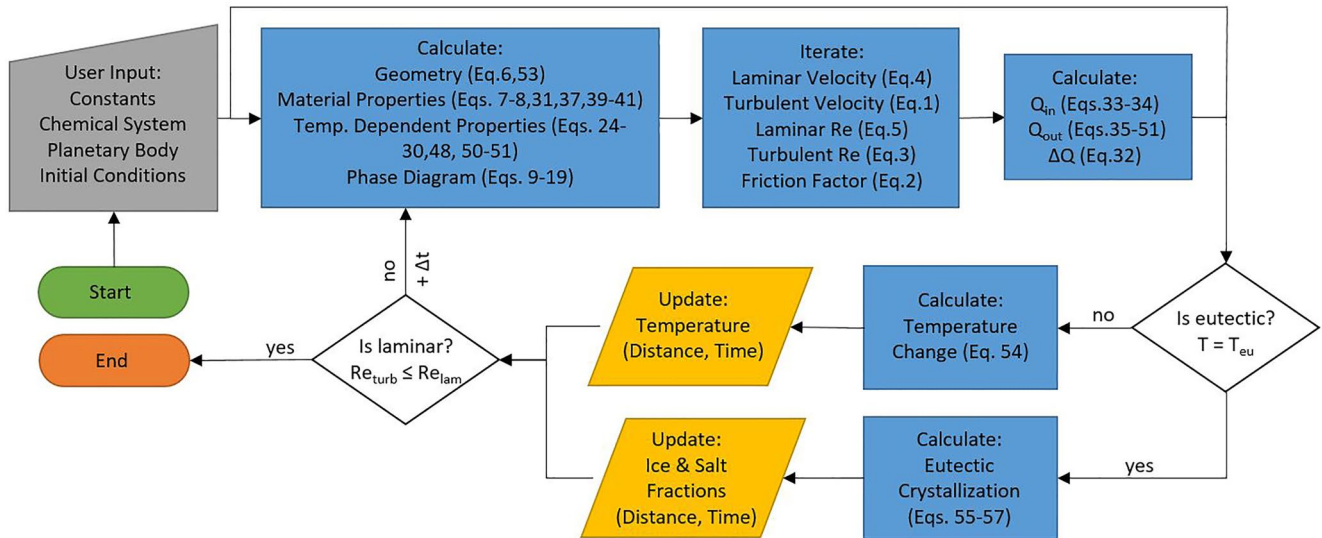
Figure 6. Flowchart demonstrating model progression and functionality. Based on initial conditions and user input, the physical, chemical, and thermal states of the flow are calculated. If the temperature of the flow does not equal the eutectic temperature, a ΔT is calculated. For the next time step, the temperature is updated and state of the flow recalculated. This continues until the eutectic is reached or laminar flow begins. If the eutectic is reached prior to laminar flow, the temperature and bulk composition will be buffered and crystallization of two phases will allow the flow to continue evolving until the transition to laminar flow is reached and the model ends.

4. Results

4.1. Establishing Turbulence and Entrainment

To demonstrate the relative effect of density and viscosity on the flow behavior, we calculated the Reynolds number (Equation 3) for defined thicknesses, densities, and viscosities and plotted them in Figure 7. Viscosity vastly outweighs density in contributing to the down-flow evolution of Reynolds number, because viscosity can change by orders of magnitude while density has a much more restricted range for any given cryolava. More importantly, this plot demonstrates that turbulence in cryolavas is likely to persist over an increase in viscosity of 2–5 orders of magnitude with the wider range occurring at greater flow thicknesses. This suggests that flows may crystallize a significant fraction of material prior to reaching the laminar flow regime.

The 0.1-m-thick flows do not remain turbulent for very long once viscosity begins increasing and are otherwise too small to be resolved based on current observational data of icy bodies. For the thicker flows where turbulence persists over a wider range of viscosity (i.e., to greater crystal contents), a Stokes number calculation demonstrates the particle sizes that are able to be entrained in a flow (Figure 8). The Stokes number (St) was calculated as follows:

$$\text{St} = \frac{\left(2\rho_{\text{ice}} + \rho_{\text{liq}}\right) u_{\text{turb}} D^2}{144\eta_{\text{bulk}} h} \tag{58}$$

where D is the particle diameter (Eaton & Fessler, 1994; Fessler et al., 1994; Zhang et al., 2016). This effectively represents the responsiveness of a particle to changes in the flow field. Particles with low Stokes numbers (St << 1) will follow the flow lines of the carrier fluid, while particles with high Stokes numbers (St >> 1) will have enough inertia to cross flow lines and not be entrained by the turbulence.

4.2. Heat Fluxes

Each of the individual heat fluxes described in Section 3.5 are plotted against distance in Figure 9. Because distances were so short for the 0.1 m thick flows, they were not plotted. We also note that since these plots are on a log scale, the initial conditions at $t = 0$ cannot be plotted. Thus, the data appear to be starting at a finite distance from the vent which is merely the results starting after the first time step. For each composition and each thickness, the Q_{vap} was at least two orders of magnitude larger than any other flux, accounting for more than 99% of the total thermal budget. The kink in the Q_{vap} curves resulted from the onset of crystallization, which progresses
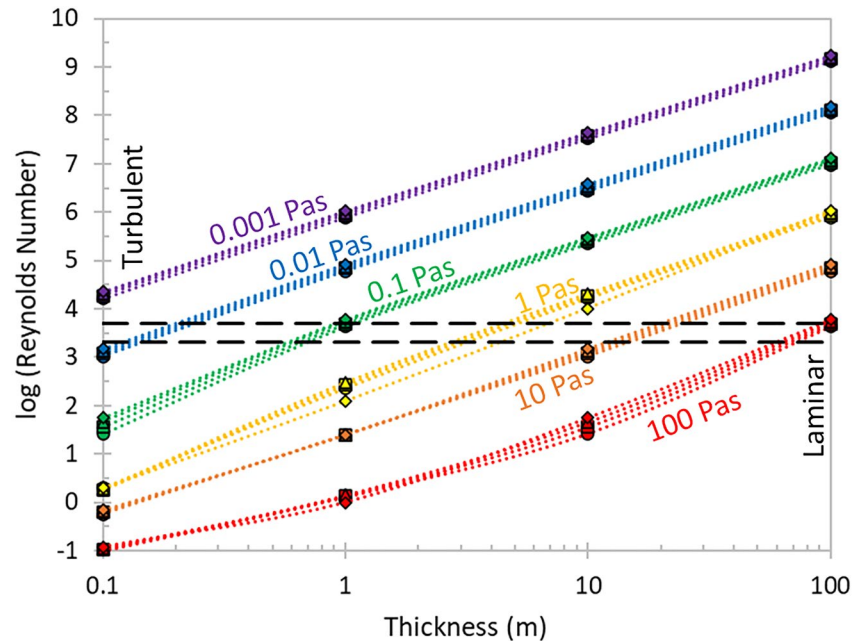
Figure 7. Flow regime of potential cryolavas of different thicknesses and viscosities. The black dashed lines represent the transition zone between turbulent and laminar flow. Color indicates viscosity: 0.001 (purple), 0.01 (blue), 0.1 (green), 1 (yellow), 10 (orange), and 100 Pa s (red). Densities are indicated by symbol shape: 900 (circles), 1,000 (squares), 1,100 (triangles), and 1,200 kg m^{-3} (diamonds). As a crude contextual comparison, the yellow curves might be analogous to komatiitic liquid and the orange curves analogous to basaltic liquid.

down temperature and further from the vent as concentration increased. At the eutectic concentration, the temperature was buffered at the eutectic temperature until solidification resulting in the horizontal line after the kink.

Only the Q_{fric} and Q_{erod} heat fluxes varied to a noticeable extent with changes in flow thickness (Figure 9). Both Q_{fric} and Q_{erod} increased by 1–1.5 orders of magnitude with each order of magnitude increase in thickness. The other three fluxes (Q_{cond}, Q_{rad}, and Q_{insol}) maintained the same order of magnitude throughout all model runs.

Since the erodibility of the surfaces of icy bodies is poorly constrained, we have included results from an order of magnitude increase in this value. Changes in the erodibility term only affected the Q_{erod} flux. As the erodibility term was increased by an order of magnitude, Q_{erod} increased by an order of magnitude as well. However, the Q_{vap} term was still orders of magnitude larger than the other fluxes, for thicknesses less than 100 m and all compositions investigated (Figure 9). For the 100 m thick flows, Q_{erod} started about an order of magnitude lower than Q_{vap}. For more dilute compositions (<10–12 wt%), this order.

Figure 8. Stokes number calculation (Equation 58) for ice crystals ($\rho = 920$ kg m^{-3}) against the particle diameter. Solid blue lines represent maximum and minimum values for flow thicknesses between 0.1 and 100 m, velocities between 0.1 and 10 m s^{-1}, and bulk viscosities between 1 and 100 mPa s. The upper solid curve represents a maximum for the thinnest, highest velocity, lowest viscosity scenario. The lower solid blue curve represents a minimum for the thickest, lowest velocity, highest viscosity scenario. Dashed lines between the solid lines represent contours of order of magnitude changes of thickness, velocity, and/or viscosity.

Of magnitude difference did not change much with increasing time or distance. For more concentrated solutions (>15 wt%), Q_{vap} decreased nearly an order of magnitude, while Q_{erod} came within a factor of four of Q_{vap}. This was the only scenario where Q_{vap} was not at least 1.5 orders of magnitude larger than all other fluxes. All other heat fluxes remained the same as previous runs.

To investigate how changes in slope might affect the results, the model was also run for an order of magnitude increase in slope. Changes in the ground slope term only impacted the Q_{fric} and Q_{erod} fluxes. Both terms were increased by ~1.5 orders of magnitude with an increase in slope from 0.1° to
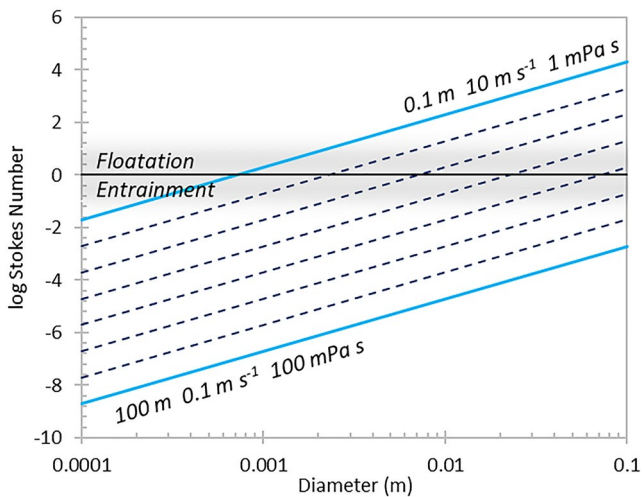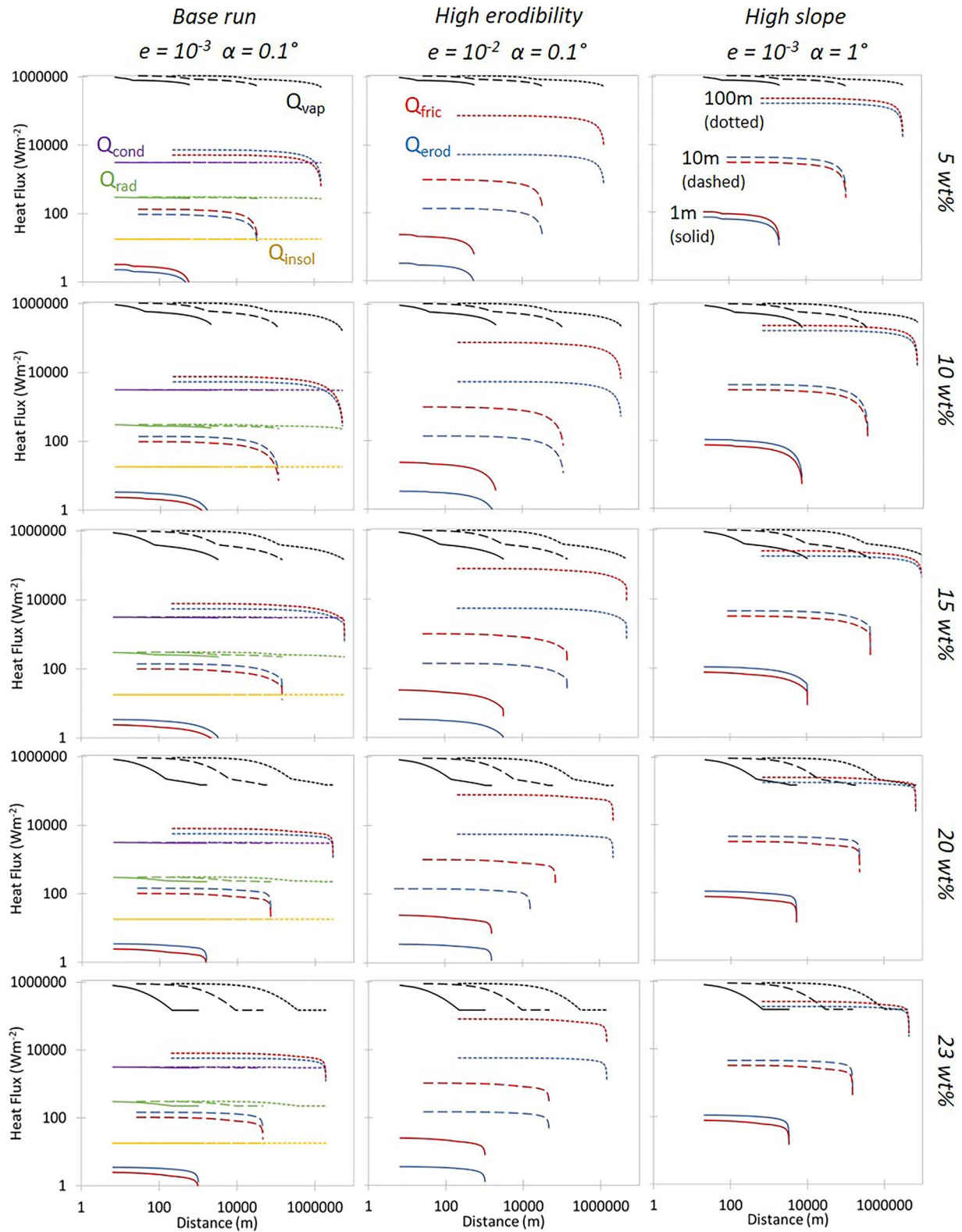
Figure 9.

$1°$ (Figure 9). This increase was only significant for the thickest of flows where the two fluxes approach 25%–50% of the Q_{vap} term, instead of being <1%. However, since Q_{fric} and Q_{erod} were of opposite sign (i.e., the former a heat gain term and the latter a heat loss term) and similar scale, they essentially canceled each other out for all compositions and thicknesses investigated. All other heat fluxes, again, remained approximately unchanged and negligible. Thus, in every scenario, the Q_{vap} flux dominated the thermal budget and was the only required heat flux for modeling the turbulent evolution of effusive cryolava flows.

4.3. Down-Flow Evolution

The model was run for initial thicknesses of 0.1, 1, 10, and 100 m and starting compositions between 5 and 23 wt% (H_2O-NaCl eutectic, Figure 4). We refer to individual model runs by initial composition and/or initial thickness. Both composition and thickness evolve throughout the model run and the reader should not assume that these initial values represent the conditions of the evolving flow at any point other than $t = 0$. The state of the flow at the turbulent to laminar transition for each model run is presented in Table 2 and plotted in Figure 10.

For 0.1-m-thick flows, it took 12–203 s to reach the transition to laminar flow at roughly 3–40 m from the vent, depending on concentration. Flow thicknesses decreased from evaporative losses between 0% and 30% with the minimum and maximum decrease being for the 5 and 15 wt% runs, respectively. For the 1-m-thick flows, the transition was reached after 630–3,600 s (10.5–60 min), 580 m–3.3 km from the vent. Thicknesses decreased between 8% and 45% with the minimum and maximum decrease being for the 23 and 10 wt% runs, respectively. The 10-m-thick flows reached the transition after 9,250–37,800 s (2.6–10.5 hr), traveling 33–146 km. Thicknesses decreased between 9% and 59% with the minimum and maximum being for the 23 and 10 wt%, runs, respectively. The 100-m-thick flows reached 1,512–5,869 km, taking 110,410–459,730 s (1.3–5.3 days) to do so. Flow thicknesses at the transition varied between 35 for 10 and 91 m for 23 wt%. Figure 11 demonstrates these results as normalized values in the context of temporal evolution. The 5 and 20 wt% scenarios were chosen as a representative of dilute and concentrated solutions with intermediate concentrations demonstrating behavior in between these endmembers. More dilute concentrations decrease in thickness more readily due to the higher water content and lower vapor pressure. However, this trend does not hold for the 0.1-m-thick flows that freeze over much shorter times and distances that do not allow as much vaporization to occur.

The model was also run for the same compositions and thicknesses but with an increased value for the erodibility term. Since this term was very poorly constrained, we saw fit to investigate how sensitive the results were to changes in this term. The erodibility value used was originally for basaltic compositions but we expect ice to have a larger erodibility than basalt. These results are presented in Table 3 and plotted in Figure 10. When we increased the erodibility of the substrate by an order of magnitude, the distance to the turbulent-laminar transition remained unchanged for the 0.1, 1, and 10 m thick flows. For the 100-m-thick flows, the distance was reduced for all concentrations, ranging from 1,276 at 5 to nearly 5,000 km at 15 wt%. The timescales for these runouts remained unchanged for the 0.1- and 1-m-thick flows and were reduced by only 45–600 s (0.5%–2%) for the 10-m-thick flows. The 100-m-thick flows were the only ones with a large change in timescale, being reduced by 20,640–188,130 s (5.7 hr–2.1 days or 22%–69%). Results for thickness remained unchanged for the 0.1-, 1-, and 10-m-thick flows, while the 100-m-thick flows were between 2 and 18 m thicker than the model runs with lower substrate erodibility.

Another parameter that may have a large impact on the results is the slope (i.e., local topography). The initial model retained a constant, near horizontal slope of $0.1°$. To investigate the sensitivity of the results to this parameter, we have also made similar model runs but with a larger slope of $1°$. These results are presented in Table 4 and plotted in Figure 10. When the slope was increased from $0.1°$ to $1°$, the distance from the vent to the transition to laminar flow increased for all concentrations and thicknesses. Distances for the 0.1 m thick flow were roughly 4–5

Figure 9. Evolution of heat fluxes along cryolava flows (see Figure 5) up to the turbulent-laminar transition showing that the effect of concentration, substrate erodibility, and slope do not change the dominant heat loss mechanism. Starting points of each curve is arbitrary due to the choice of time step and inability to plot from zero distance in a log scale. (left) Fluxes are plotted for the initial model run with erodibility $e = 10^{-3}$ and slope $\alpha = 0.1°$. Fluxes are plotted for 1 m thick (solid lines), 10 m thick (dashed lines), and 100 m thick (dotted lines) flows. Q_{vap} is plotted in black, Q_{cond} is plotted in purple, Q_{rad} is plotted in green, Q_{erod} is plotted in blue, Q_{fric} is plotted in red, and Q_{insol} is plotted in yellow. (middle) Fluxes are plotted for a model run with $e = 10^{-2}$ and $\alpha = 0.1°$. Q_{insol}, Q_{rad}, and Q_{cond} have been left off these graphs for clarity. Only the fluxes that have been affected by the changes in e or α have been plotted, along with Q_{vap} for context. (right) Fluxes are plotted for a model run with $e = 10^{-3}$ and $\alpha = 1°$. Q_{insol}, Q_{rad}, and Q_{cond} have been left off these graphs for clarity. Results for a 5 wt% starting solution are plotted in the top row and 23 wt% starting solution on the bottom row with intermediate compositions in the interstitial rows.

Table 2
Physical Conditions of the Flow at the Turbulent to Laminar Transition

Initial thickness	Time	Distance from vent	Bulk salinity	Transition temperature	Flow thickness	Ice fraction	Salt fraction	Eroded fraction	Solid fraction	Flow velocity	Bulk viscosity	Yield strength
h_0 (m)	t (s)	d (km)	X (wt frac)	T (K)	h (m)	φ_{ice} (vol frac)	φ_{salt} (vol frac)	$\Sigma\varphi_{erod}$ (vol frac)	φ_{total} (vol frac)	u (m s^{-1})	η_{bulk} (Pa s)	σ_y (Pa)
$X_0 = 5$ wt% $T_0 = 273$ K												
0.1	12	0.003	0.09	267	0.10	0.48	–	0.00	0.48	0.2	0.036	13
1	630	0.58	0.11	266	0.77	0.57	–	0.00	0.57	0.5	0.867	34
10	9,250	33	0.12	265	6.8	0.62	–	0.00	0.62	1.5	23.2	55
100	112,990	1,512	0.13	264	62	0.65	–	0.00	0.65	4.6	650	75
$X_0 = 10$ wt% $T_0 = 273$ K												
0.1	97	0.02	0.16	261	0.08	0.42	–	0.00	0.42	0.2	0.030	7
1	2,485	2.0	0.20	257	0.55	0.54	–	0.00	0.54	0.4	0.561	21
10	37,800	114	0.22	254	4.1	0.60	–	0.00	0.60	1.2	11.6	37
100	459,730	5,128	0.23	252	35	0.62	–	0.01	0.64	3.4	283	47
$X_0 = 15$ wt% $T_0 = 273$ K												
0.1	203	0.04	0.21	255	0.07	0.35	–	0.00	0.35	0.2	0.029	3
1	3,600	3.3	0.23	252	0.61	0.52	0.02	0.00	0.54	0.5	0.654	15
10	36,710	146	0.23	252	6.1	0.57	0.03	0.00	0.60	1.4	20.7	26
100	368,580	5,869	0.23	252	61	0.60	0.03	0.01	0.64	4.5	657	32
$X_0 = 20$ wt% $T_0 = 273$ K												
0.1	124	0.03	0.23	252	0.09	0.33	0.03	0.00	0.35	0.2	0.037	2
1	1,520	1.6	0.23	252	0.87	0.49	0.06	0.00	0.55	0.6	1.02	11
10	16,150	72	0.23	252	8.6	0.54	0.07	0.00	0.61	1.7	35.5	18
100	164,720	2,890	0.23	252	86	0.57	0.07	0.01	0.65	5.3	1,107	23
$X_0 = 23$ wt% $T_0 = 273$ K												
0.1	72	0.02	0.23	252	0.09	0.31	0.05	0.00	0.37	0.2	0.041	2
1	980	1.0	0.23	252	0.92	0.47	0.08	0.00	0.55	0.6	1.11	8
10	10,645	46	0.23	252	9.1	0.52	0.09	0.00	0.61	1.7	38.8	14
100	110,410	1,898	0.23	252	91	0.55	0.09	0.00	0.65	5.5	1,211	18

Note. The time step used was 1 s for 0.1-m-thick flows, 5 s for 1 and 10-m-thick flows, and 10 s for 100-m-thick flows. The initial temperature of the solution was 273 K for each run.

times longer, 1 and 10 m thick flows were roughly 3 times longer, and 100 m thick flows were between 1.5 and 2.5 times longer. The emplacement timescales of the 01 m thick flows were 15%–158% longer, the 1-m-thick flows were 1%–26% longer, the 10-m-thick flows were 1%–10% longer, and the 100-m-thick flows were 26%–64% shorter. The calculated thickness at the turbulent to laminar transition was either thinner or essentially the same as the results from the shallower slope for 0.1-, 1-, and 10-m-thick flows, ranging from 1 mm–30 cm thinner. The 100 m thick flows were between 2 and 32 m thicker.

4.4. Turbulent to Laminar Transition

For the model runs of 5 and 10 wt%, the temperature of the transition to laminar flow was above the eutectic and decreased with increasing thickness (Table 2). While the eutectic temperature (252 K, Figure 4) was technically reached by the 10 wt%, 100 m thick flow, no salt crystallization actually occurred prior to the end of the model. For these model runs, and the 15 wt%, 0.1-m-thick run, the bulk compositions evolved toward more concentrated solutions as water-ice crystallized, increasing the solid fraction and viscosity enough to reach the transition to laminar flow prior to evolving chemically to the eutectic. All subsequent model runs reached the eutectic, and
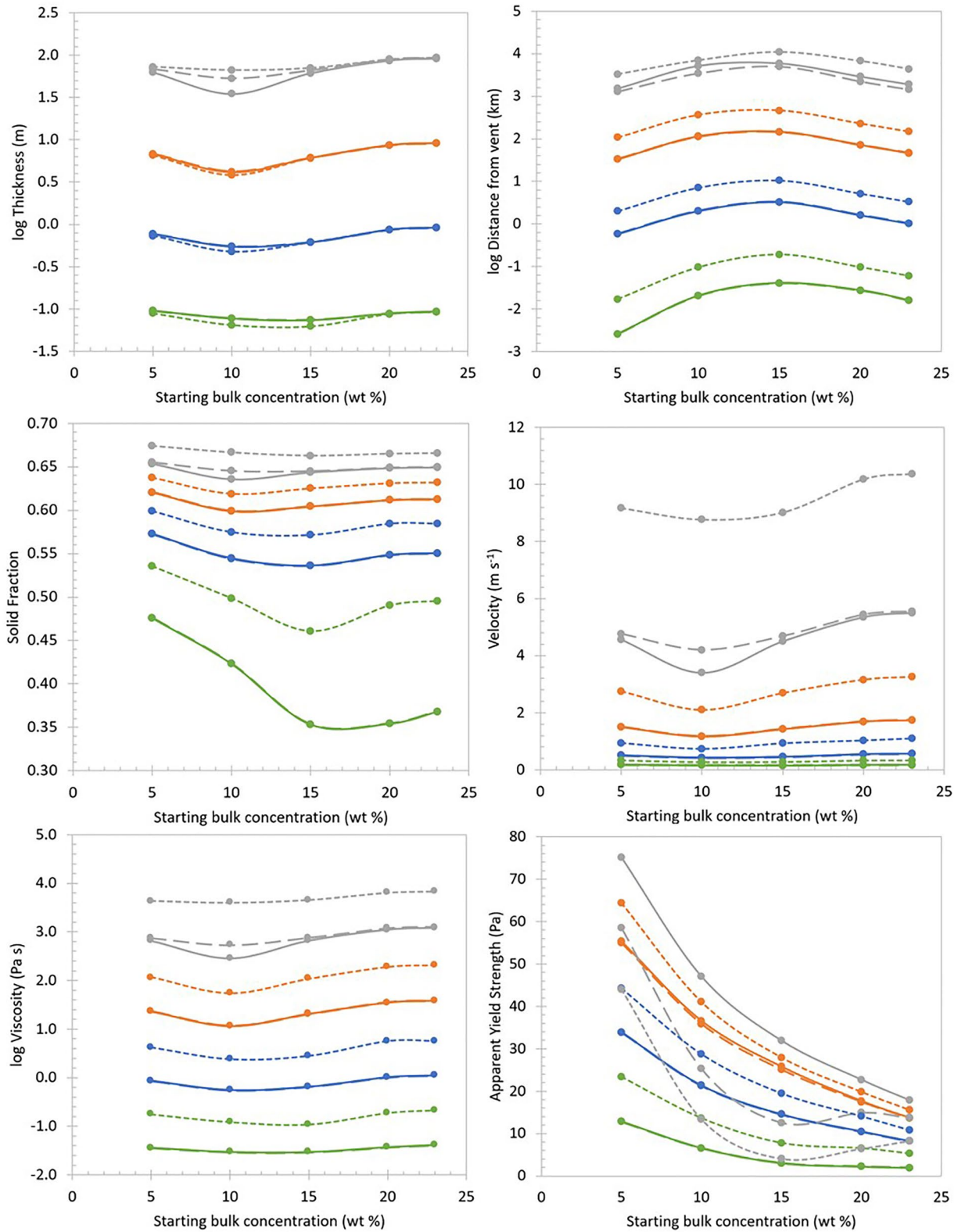
Figure 10. Plots of results from Tables 2–4 showing model output values of the physical conditions of the flow at the turbulent to laminar transition with interpolated curves for 0.1 (green), 1 (blue), 10 (orange), and 100 m (gray) initial flow thicknesses. Solid curves are data from Table 2, long-dashed curves are higher erodibility data from Table 3, and short-dashed curves are higher slope data from Table 4. Slope has a stronger control on the results than does substrate erodibility.
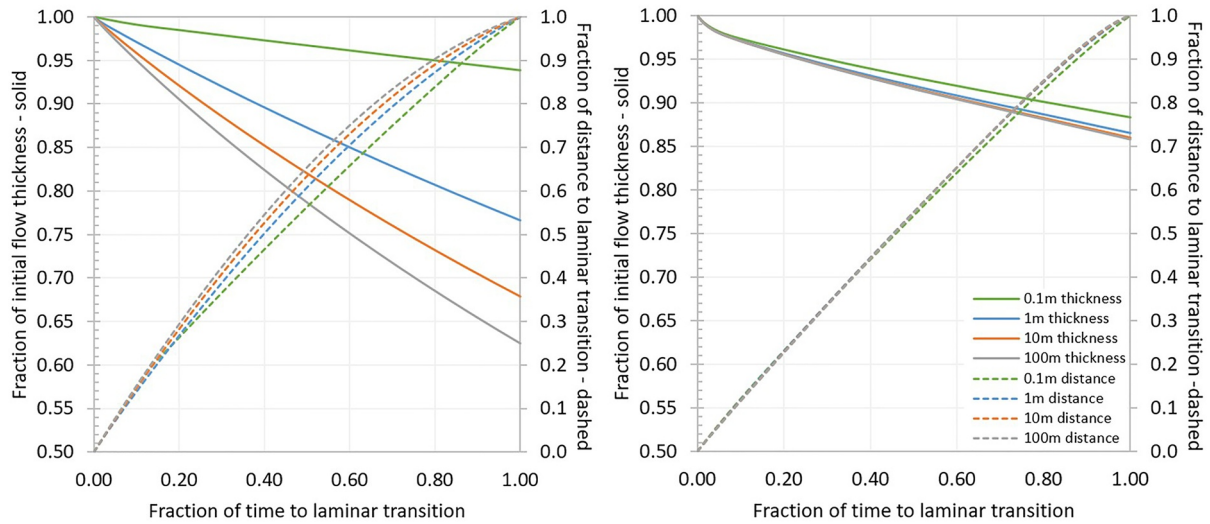
Figure 11. Representative evolution of flow thickness (solid lines) and distance (dashed lines) as a function of time for the 5 (left) and 20 wt% (right) scenarios for 0.1 (green), 1 (blue), 10 (orange), and 100 m (gray) initial flow thicknesses. Thickness, distance, and time are all normalized to the end transition to the laminar regime to allow each initial flow thickness to be directly compared. The legend applies to both graphs. These demonstrate similar temporal evolution. More dilute concentrations vaporize more material, and distance evolves in a similar linear fashion irrespective of concentration.

thus, the transition temperature was constant for each of these scenarios (Table 2). As crystallization occurred and the composition of the liquid evolved, the bulk salinity of the liquid was consistent with the transition temperature as well, that is, when the temperature was buffered at the eutectic, the bulk salinity remained at the eutectic composition. The eutectic was reached for all investigated thicknesses at compositions >15 wt%.

The amount of crystallization that occurred before the transition to laminar flow was approximately independent of concentration, but strongly dependent on flow thickness. The 0.1-m-thick flows achieved 40 ± 11, the 1-m-thick flows achieved 55 ± 3, the 10-m-thick flows achieved 61 ± 2, and the 100-m-thick flows achieved 65 ± 1 vol% (Table 2). The amount of crystallization resulted in bulk viscosity increases of approximately an order of magnitude (~0.01) for 0.1-m-thick flows, three orders of magnitude (~1) for 1-m-thick flows, four orders of magnitude (~10) for 10-m-thick flows, and 5.5–6 orders of magnitude (~300–1,000 Pa s) for 100-m-thick flows from an initial viscosity of ~1 mPa s. At compositions around ~10 wt%, there was a bulk viscosity minimum and compositions both more dilute and more concentrated tended to have higher bulk viscosities at the transition to laminar flow (Figure 10). This minimum became less pronounced with decreasing thickness and was no longer distinguishable at 0.1 m thickness. Flow velocities at the transition mirror the viscosity trends with a minimum at 10 wt%. The 0.1-m-thick flows reached 0.17 ± 0.02, the 1-m-thick flows reached 0.50 ± 0.12, the 10-m-thick flows reached 1.5 ± 0.5, and the 100-m-thick flows reached 4.7 ± 1.7 m s^{-1}. For each composition, the velocity increased by approximately a factor of three for each order of magnitude increase in thickness.

Changing the erodibility of the substrate did not significantly change the results for the 0.1-, 1-, and 10-m-thick scenarios at any composition (Table 3). The main influence of changing this parameter was observed to dampen the 10 wt% minima observed in viscosity, velocity, and thickness for the 100-m-thick flow scenario (Figure 10).

Changing the slope from 0.1° to 1° had a stronger effect on the results. The viscosity of the turbulent to laminar transition increased for every composition and thickness by roughly half an order of magnitude (Figure 10). For 10 wt% and 100 m thickness, it was closer to a full order of magnitude increase. The viscosity increase was accompanied by a 1–3 vol% increase in solid fraction at all thicknesses with the 0.1-m-thick case being much larger (6–14 vol% increase). Despite increasing the erodibility of the substrate, it was the increase in slope that had a larger effect on the amount of material eroded (Tables 3 and 4). The eroded material roughly doubled for the increased slope over the increased erodibility. For the 15 wt% 100-m-thick flow, enough material was eroded that the turbulent to laminar transition was achieved even before the eutectic temperature was reached. Velocity, in turn, roughly doubled across thicknesses and compositions (Table 4). Yield strengths also increased by roughly 2 times for 0.1-m-thick flows, 1.5 times for 1-m-thick flows, and 1.25 times for 10-m-thick flows. For the 100-m-thick flows, yield strengths decreased in a nonuniform way with a larger decrease at the more dilute

Table 3
Sensitivity of Results to an Order of Magnitude Larger Erodibility (10^{-2}), Showing Minor Changes From the Results in Table 2

Initial thickness	Time	Distance from vent	Bulk salinity	Transition temperature	Flow thickness	Ice fraction	Salt fraction	Eroded fraction	Solid fraction	Flow velocity	Bulk viscosity	Yield strength
						φ_{ice}	φ_{salt}	$\Sigma\varphi_{erod}$	φ_{total}	u		
h_0 (m)	t (s)	d (km)	X (wt frac)	T (K)	h (m)	(vol frac)	(vol frac)	(vol frac)	(vol frac)	(m s^{-1})	η_{bulk} (Pa s)	σ_y (Pa)
$X_0 = 5$ wt% $T_0 = 273$ K												
0.1	12	0.003	0.09	267	0.10	0.48	–	0.00	0.48	0.2	0.036	13
1	630	1	0.11	266	0.77	0.57	–	0.00	0.57	0.5	0.868	34
10	9,205	33	0.12	265	6.8	0.62	–	0.00	0.62	1.5	23.3	55
100	92,350	1,276	0.12	265	68	0.63	–	0.03	0.66	4.8	744	59
$X_0 = 10$ wt% $T_0 = 273$ K												
0.1	97	0.02	0.16	261	0.08	0.42	–	0.00	0.42	0.2	0.030	7
1	2,480	2	0.19	257	0.55	0.54	–	0.00	0.54	0.4	0.556	21
10	37,200	113	0.22	254	4.2	0.60	–	0.00	0.60	1.2	11.8	36
100	271,600	3,465	0.20	256	53	0.56	–	0.08	0.65	4.2	536	25
$X_0 = 15$ wt% $T_0 = 273$ K												
0.1	203	0.04	0.21	255	0.07	0.35	–	0.00	0.35	0.2	0.029	3
1	3,600	3	0.23	252	0.61	0.52	0.02	0.00	0.54	0.5	0.655	15
10	36,625	146	0.23	252	6.1	0.57	0.03	0.00	0.60	1.4	20.5	25
100	319,020	4,997	0.23	252	66	0.50	0.02	0.13	0.65	4.7	758	13
$X_0 = 20$ wt% $T_0 = 273$ K												
0.1	124	0.03	0.23	252	0.09	0.33	0.03	0.00	0.35	0.2	0.037	2
1	1,520	2	0.23	252	0.87	0.49	0.06	0.00	0.55	0.6	1.02	11
10	16,075	72	0.23	252	8.6	0.54	0.07	0.00	0.61	1.7	35.5	17
100	126,000	2,219	0.23	252	89	0.53	0.06	0.06	0.65	5.4	1,179	15
$X_0 = 23$ wt% $T_0 = 273$ K												
0.1	72	0.02	0.23	252	0.09	0.31	0.05	0.00	0.37	0.2	0.041	2
1	980	1	0.23	252	0.92	0.47	0.08	0.00	0.55	0.6	1.12	8
10	10,590	46	0.23	252	9.1	0.52	0.09	0.00	0.61	1.7	38.2	14
100	83,180	1,428	0.23	252	93	0.52	0.09	0.04	0.65	5.6	1,266	14

Note. Physical conditions of the flow at the turbulent to laminar transition with a time step of 1, 5, 5, and 10 s, respectively, for 0.1, 1, 10, and 100 m thick flows. The initial temperature of the solution was 273 K for each run.

concentrations (Figure 10). The increase in slope tended to decrease the thickness for more dilute compositions; however, this effect was dampened with larger initial thicknesses. The effect was indistinguishable for the 10-m-thick flows and the opposite effect was observed in the 100-m-thick flows, where the minimum at 10 wt% was erased as the thickness was nearly double from the initial result.

5. Discussion

5.1. Thermal Budget

The Q_{insol} and Q_{fric} fluxes comprised the entirety of the Q_{gain} term, both of which account for less than 0.1% of the total thermal budget for any investigated flow thickness. The assumption made in Section 3.5 about the incident insolation being roughly equivalent to the solar constant is therefore moot. Weaker insolation for icy bodies at a greater distance from the Sun, such as Enceladus or Pluto, will be even less important. Similarly, the assumption of head loss being completely converted to heat for Q_{fric} is also unimportant. The frictional heating term was either many orders of magnitude less than the largest heat flux or canceled out by the Q_{erod} flux.

Table 4
Sensitivity of Results to a Steeper Slope (1°), Demonstrating a Larger Change Between Results From Table 2 Than Is Found in Table 3

Initial thickness	Time	Distance from vent	Bulk salinity	Transition temperature	Flow thickness	Ice fraction	Salt fraction	Eroded fraction	Solid fraction	Flow velocity	Bulk viscosity	Yield strength
h_0 (m)	t (s)	d (km)	X (wt frac)	T (K)	h (m)	φ_{ice} (vol frac)	φ_{salt} (vol frac)	$\Sigma\varphi_{erod}$ (vol frac)	φ_{total} (vol frac)	u (m s^{-1})	η_{bulk} (Pa s)	σ_y (Pa)
$X_0 = 5$ wt% $T_0 = 273$ K												
0.1	31	0.02	0.10	267	0.09	0.54	–	0.00	0.54	0.33	0.176	23
1	760	2	0.11	265	0.73	0.60	–	0.00	0.60	0.94	4.22	44
10	10,220	108	0.12	265	6.5	0.64	–	0.00	0.64	2.8	117	64
100	76,850	3,280	0.11	266	73	0.60	–	0.08	0.67	9.2	4,385	44
$X_0 = 10$ wt% $T_0 = 273$ K												
0.1	174	0.1	0.18	259	0.06	0.50	–	0.00	0.50	0.27	0.122	14
1	3,130	7	0.21	256	0.48	0.57	–	0.00	0.57	0.74	2.43	29
10	41,360	365	0.22	253	3.8	0.61	–	0.01	0.62	2.1	55.2	41
100	165,880	7,000	0.18	259	66	0.50	–	0.17	0.67	8.8	4,020	13
$X_0 = 15$ wt% $T_0 = 273$ K												
0.1	350	0.2	0.23	252	0.06	0.45	0.01	0.00	0.46	0.28	0.109	8
1	3,635	10	0.23	252	0.61	0.55	0.02	0.00	0.57	0.93	2.83	20
10	36,910	461	0.23	252	6.1	0.58	0.03	0.01	0.63	2.7	108	28
100	256,010	10,957	0.22	253	70	0.39	–	0.28	0.66	9.0	4,576	4
$X_0 = 20$ wt% $T_0 = 273$ K												
0.1	143	0.1	0.23	252	0.09	0.44	0.05	0.00	0.49	0.33	0.188	7
1	1,570	5	0.23	252	0.86	0.52	0.06	0.00	0.58	1.0	5.67	14
10	16,445	229	0.23	252	8.6	0.56	0.07	0.01	0.63	3.2	188	20
100	122,630	6,717	0.23	252	89	0.44	0.05	0.18	0.67	10.2	6,449	6
$X_0 = 23$ wt% $T_0 = 273$ K												
0.1	91	0.1	0.23	252	0.09	0.42	0.07	0.00	0.50	0.33	0.213	5
1	1,030	3	0.23	252	0.91	0.50	0.09	0.00	0.58	1.1	5.71	11
10	10,955	149	0.23	252	9.1	0.54	0.09	0.00	0.63	3.3	204	16
100	81,970	4,363	0.23	252	93	0.47	0.08	0.11	0.67	10.4	6,861	8

Note. Physical conditions of the flow at the turbulent to laminar transition with a time step of 1, 5, 5, and 10 s, respectively, for 0.1-, 1-, 10-, and 100-m-thick flows. The initial temperature of the solution was 273 K for each run.

Since cryolava flows are cold, it is perhaps unsurprising that the radiative cooling term was a minor contribution to the thermal budget, representing less than 0.1% of the total thermal budget. Furthermore, the conductive heat loss through the base (Q_{cond}) was a fraction of a percent, despite being an overestimation, suggesting that our assumption of a 0.2-m-thick thermal boundary layer is also moot. While all of these fluxes remained in our calculations for consistency, and to allow for their use in other scenarios, we suggest that they can generally be neglected in order to simplify calculations for future models of cryolava flows of similar composition. Taken together, the thermal budget could be simply calculated by

$$\Delta Q = Q_{vap} \left(+ Q_{erod} - Q_{fric}\right) \tag{59}$$

where there are no heat gain terms, and cooling is controlled by vaporization. This is demonstrated by the relative sizes of the arrows representing the heat fluxes in Figure 5. For flows thicker than ~10 m, heat loss to eroded substrate (xenoliths) and frictional heat gain should also be included (Figure 9). These two terms tend to evolve together, but one can dominate over the other for certain conditions. Together, the three terms include more than 99% of the thermal budget for all concentrations and thicknesses investigated.

Table 5
Aspect Ratios (Length:Thickness) for Each of the Model Runs

wt%	Erodibility = 10^{-3} slope = 0.1°				Erodibility = 10^{-2} slope = 0.1°				Erodibility = 10^{-3} slope = 1°			
	0.1 m	1 m	10 m	100 m	0.1 m	1 m	10 m	100 m	0.1 m	1 m	10 m	100 m
5	27	750	4,909	24,198	27	750	4,880	18,678	192	2,729	16,611	45,142
10	267	3,700	27,684	147,118	267	3,692	27,008	65,131	1,478	14,870	95,246	105,458
15	553	5,361	23,981	96,397	553	5,360	23,882	75,721	3,064	17,088	75,945	156,017
20	312	1,853	8,355	33,685	312	1,853	8,311	24,952	1,103	5,968	26,656	75,400
23	173	1,115	5,109	20,924	173	1,115	5,081	15,386	653	3,622	16,375	46,970

Note. These aspect ratios are that of the turbulent section of the flow and may differ from the final morphology that includes the laminar evolution.

5.2. Flow Geometry and Timescales

The 5 wt% NaCl liquid always underwent the turbulent to laminar transition at the shortest distance from the vent, while the 15 wt% NaCl liquid always transitioned at the greatest distance. This pattern also generally holds true for the timescales of transition to laminar flow, with the exception of the 100 m thick flow for 23 wt%, which reached the transition earlier despite covering a greater distance than the 5 wt% flow. This is likely due to the larger amount of eroded material incorporated into the flow that drives viscosity higher earlier in its evolution. At the other end of the spectrum, the 10 wt% 10-m-thick and 100-m-thick flows took the longest time to reach the transition despite being shorter than the 15 wt% flows of the same initial thicknesses. This is likely caused by the evaporative mass loss rate being higher for the 10 wt% flows. These flows reduce in thickness the most and therefore also slow down the most from their initial velocity. The 5 and 15 wt% flows lost the least and most material, respectively, for the 0.1-m-thick flows, but for all other thickness, the 23 flow lost the least and the 10 wt% lost the most. This is likely the cause of the minimum in several parameters observed in Figure 9 for 10 wt%.

As the material is lost from the system from vaporization in the low-pressure environment, the thickness of the flow in each run ultimately decreases as well. If the flow reaches the eutectic, then the flow will decrease thickness by a similar percentage for a given concentration irrespective of initial thickness. For compositions that do not reach the eutectic (i.e., <12–15 wt%), the thicker flows tend to lose a larger percentage of the initial thickness. Again, a minimum thickness (alternatively, a maximum loss) exists at 10 wt% where only 55%, 41%, and 35% of the flow thicknesses are retained for 1, 10, and 100 m initial thicknesses, respectively. This minimum is not observed in the 0.1-m-thick runs. Both more dilute and more concentrated compositions retain larger percentages of the initial thickness. The observed minima correspond with the longest timescales of emplacement, that is, the longer the timescale, the more material is lost through vaporization.

The aspect ratios (length:thickness) can be used as a description of feature morphology. Aspect ratios calculated for each model run are presented in Table 5. Calculating this parameter allows us to begin drawing comparisons to observable features. If we find that many flows (flow-like features) have higher aspect ratios than our model predicts, this suggests that either the laminar flow regime adds significant length to the flow or tube formation may play a role in emplacement.

Features on Europa interpreted as cryovolcanic in origin tend to be domes (Figure 1a) or low-albedo, smooth deposits. Typical domes on Europa range from 3 to 10 km across with 40–100 m heights resulting in aspect ratios of ~30–100, which are much smaller than we have calculated here (Fagents, 2003). However, domes are an inappropriate comparison to the types of flows we modeled, as they do not represent low viscosity, turbulent flows. Dome emplacement, as modeled by Quick et al. (2017), requires starting viscosities at least five orders of magnitude larger than the starting material we used, meaning that they were certainly never turbulent. The low-albedo, smooth deposits tend to occupy low lying terranes, show lobate morphology, and appear to be the result of low-viscosity flooding (Fagents, 2003). However, the aspect ratios of these features cannot be determined because they are topography-limited flows, that is, they fill basins and depressions so any thickness information would not represent a true flow thickness but merely a depth of infill. Until higher spatial resolution imagery is available to identify smaller, thinner, and/or narrower features on Europa, we must look at other bodies for a morphological comparison to our model results.

The next logical location to investigate would be the asteroid Ceres, which may also have effusions of chloride-rich brines (Ruesch et al., 2019; Thomas et al., 2019). Several flow features are present in craters (e.g., Occator and Haulani) that have been considered cryovolcanic as they appear to emanate from a source region and flow direction can be against the topographic gradient (Krohn et al., 2016). Lengths of these flows range from 0.5 to 20 km but thicknesses are poorly constrained. If the thickness of these flows is between 10 and 100 m, the aspect ratio could range from 5 to as high as 2,000, still slightly lower values than our model predicts. This could be explained by a compositional difference (flows on Ceres likely have carbonate and sulfate components) or by the flows being volume limited (flow arrests due to loss of mass flux rather than freezing in place, resulting in shorter flows).

Additionally, we draw another comparison to Mohini Fluctus (Figure 1c) on Titan as one of the most convincing cryovolcanic flow morphologies described. The length of the flow is roughly 140–180 km depending on the exact starting and ending points used. Flow thickness has been inferred to be tens of meters thick based on age and stratigraphic relations to surrounding dunes (Lopes et al., 2013). If we use 10–50 m as thickness estimates, the aspect ratio ranges from 2,800 to 18,000, consistent with the scale of the aspect ratios of our 10 m thick model results. We note that our model is inappropriate for flows on Titan as the presence of an atmosphere should reduce evaporative losses and introduce convective heat losses dramatically changing the thermal budget. However, the flow feature on Titan is likely the closest morphology to that predicted by our model. We also note that final flow dimensions will likely be larger than predicted by this model, because it terminates at the turbulent to laminar transition and not at the final flow length.

5.3. Turbulent to Laminar Transition

Many cryolavas are likely to be aqueous brines, predominantly crystallizing water ice upon cooling below the liquidus. Due to the turbulent nature of the low viscosity material, the heat loss will distribute evenly throughout the flow resulting in a supercooled liquid. Temperature gradients at the top and base of the flow will result in ice crystallization locally at each boundary, while the turbulent supercooled liquid also promotes ice nucleation (Makkonen & Tikanmäki, 2018). In turbulent waters, ice forms as fine, suspended crystals commonly referred to as frazil (Tsang & Hanley, 1985). These fine particles will remain in suspension acting to increase the viscosity of the flow. However, in supercooled water, the ice particles have adhesive properties (Tsang, 1982) and will tend to flocculate/agglomerate as they collide in the turbulence (Reeks, 2014; Stickler & Alfredsen, 2009). Ice flocculates/agglomerates will attach to the substrate forming a layer of anchor ice (Stickler & Alfredsen, 2009; Tsang, 1982). This anchor ice formation is facilitated by the turbulence, which helps to counteract the buoyancy effects of the less dense particles. However, for briny composition (i.e., higher salinity), these adhesive properties are diminished (Hanley & Tsang, 1984; Tsang & Hanley, 1985). Our model does not account for anchor ice deposition/accumulation, which could be important for pure water flows. However, we expect a higher brine content in erupted cryolava, and thus, diminished adhesive properties of the crystallizing phase(s).

Flocculation/agglomeration of particles is also not considered in this model. This could be a mechanism that allows formation of a carapace, or even cryolava tubes, in the turbulent regime prior to transitioning to laminar flow. If the individual crystals grow in size or accumulate together, the particle diameter (or effective diameter) could become large enough to no longer be entrained in the flow (i.e., large Stokes number). With such large particles (>~1 cm), fractionation of the solid volume fraction would be possible, resulting in rafts of ice on top of the turbulent flow (Figure 8). This may result in flow insulation/isolation from the low-pressure environment closer to the vent than predicted by our model, ultimately leading to longer-lived flows in both distance and time. Efficient crystal floatation would also influence the flow viscosity. The physical effect on the bulk viscosity of adding crystals tends to be larger than the effect of changing temperature or changing composition from forming crystals. Crystal fractionation would essentially remove this physical effect, suggesting that the viscosity of the remaining fluid would increase much more slowly, and runout distances may increase.

Once flows reach the transition to laminar flow, we predict that there will be a large volume fraction of entrained solids, ~55%–67% (Tables 2–4). There are several options for flow behavior once this transition is reached. The first option would be for Stokes' Law floatation and fractionation of the solids to occur rapidly, creating an insulating carapace atop the flow. This very well may be the mechanism that allows cryolava tubes to form. However, at roughly 60 vol% solids at the transition, the size of the tube would likely be small. If tubes were to form, the separation of solids would likely lead to re-initiation of turbulence in the remaining flowing liquid. Another

possibility is that the flow would evolve and persist as a slush, advancing much like an "a" a flow until complete solidification. Alternatively, it is possible that the flow would be choked by the large solid fraction, so that the laminar flow regime would not last very long in time or distance. If the crystals form an interlocking framework, increasing the yield strength, the remaining liquid phase may be able to drain from the flow. This may manifest in the form of moats or icings around the peripheries of the flow front. If draining of the liquid does not occur, inflation may dominate until the rupture of the crystal framework occurs. These ruptures may heal themselves as the exposed liquid rapidly boils away or a breakout lobe may spawn perpetuating flow advance. This would be highly dependent on the mass flux being maintained at that distance from the vent.

Conditions in/of the conduit would have a strong control over downflow evolution. One example would be an initial flow velocity imposed from the flux out of the vent. This could result in higher starting velocities than modeled here, implying larger Reynolds numbers, longer distances to the turbulent to laminar transition, and/or higher mechanical erosion rate (more erosive power). However, understanding the state and evolution of the conduit would require an entire modeling effort itself, which we did not attempt to broach in this work.

5.4. Cryolava Tube Formation?

The motivation for creating this model was to develop a new model for the turbulent emplacement of cryovolcanic flows in low temperature and low-pressure environments that does not assume the flow to be roofed by solid ice from its initiation. The results allow us to investigate more closely the feasibility of lava tubes as an emplacement mechanism in cryovolcanic contexts. Our results suggest that potential cryolava flows could remain turbulent for over 100 km and with crystal contents up to 60%–65% (Tables 2–4). Flows would then likely have crystallized too much before reaching the point where a stable roof could form and tubes initiate. However, this does not preclude the possibility of earlier roof formation in the turbulent regime. Flocculation, agglomeration, or even just crystal growth (as mentioned in Section 5.3) could result in particles large enough to no longer be entrained, resulting in Stokes' Law separation (floatation) of those particles and a transition to something more like Figure 2. The floatation of many large particles could potentially form a roof/carapace that begins to resemble something like a lava tube, assuming enough particle flotation occurs to create a roof of requisite thickness (0.25–0.5 m) to hold up against the vapor pressure of the fluid. Such a scenario drastically changes the material property evolution from the results of this model. Fractionation of the solids in the flow would mean that the rheology no longer evolves as quickly and the vaporization is restricted. Maintaining a low viscosity and eliminating the largest heat flux cooling the flow suggests that it may travel faster and/or farther than modeled here.

Cryolava tubes would likely require large volumes of erupted material, either to form thick enough flows or to allow regular pulses that travel through preferred pathways essentially forming a tube out of multiple flow units (e.g., Gregg, 2017; Roberts & Gregg, 2019). Because of the difficulties in amassing large quantities of liquid in an ice shell, large volumes of cryomagma are not expected (Lesage et al., 2020). Thus, evidence for effusive cryovolcanism (let alone large-scale) is expected to be rare.

5.5. Silicate—Cryolava Comparisons

Silicate liquids will not boil in the low-pressure environment, so the crust on top of the flow forms mainly by radiative heat loss at the interface. Cryolavas are much colder and do not lose significant heat through radiation (Figure 9). Instead, they lose heat predominantly through vaporization. In both cases, roof formation would act to inhibit or eliminate the largest sources of heat loss from the flow, allowing emplacement over longer distances and/or durations. Models of silicate lavas suggest that high effusion rates ($>10\,m^3\,s^{-1}$) tend to inhibit crust formation as the shear rates become larger, for a constant channel geometry, promoting crustal breakup (Gregg, 2017; Kerr et al., 2006; see; Sauro et al., 2020). For cryolavas, high effusion rates are a requirement for roof formation to overcome the loss of material vaporized in the low-pressure environment.

The eruptive temperatures of silicate lavas are much greater than the solidus of the substrate (assuming roughly similar composition of substrate and lava). Silicate lavas typically have hundreds of degrees between the liquidus and solidus temperatures. Cryolavas may erupt superheated by several degrees but the temperature gradient between the cryolava and the substrate is much smaller. Natural cryolavas are likely to have a more complicated composition than we model here, lending itself to a wider subliquidus (i.e., partially crystallized) range; however, less than ~120 K difference between solidus and liquidus is likely to exist (e.g., the H_2O-NH_3-CH_3OH eutectic

(Kargel et al., 1991)). In the case of a water-dominated liquid flowing on a water-ice-dominated substrate, the liquidus of the cryolava and the melting temperature of the substrate are similar. This suggests that cryolavas will have an even more difficult time downcutting and eroding channels than silicate lavas, which themselves struggle to do so efficiently under most conditions (Greeley et al., 1998).

Turbulence is only expected to exist in silicate flows with unusually low viscosity, due to very high temperatures and/or strongly depolymerized compositions (i.e., komatiites and carbonatites) or topographically confined channels (Griffiths, 2000). Turbulence will be more prevalent in cryolavas, which have orders of magnitude lower liquidus viscosities (1–3 mPa s) than silicate liquids (10–30 Pa s for mafic compositions (Chevrel et al., 2014; Kolzenburg et al., 2018; A. A. Morrison et al., 2019; Sehlke & Whittington, 2015; Sehlke et al., 2014)). Since cryolavas have lower viscosities, turbulence can be achieved in much thinner flows (Figure 7). However, thinner flow units have smaller thermal masses (per unit area) and lose heat too quickly to attain kilometer-scale flow lengths. Our model predicts that 10-m-thick flows can reach distances of over 100 km for even simple compositions (Tables 2–4); similar to what is observed at Doom Mons (Mohini Fluctus) on Titan (Figure 1). This could be a function of composition, where a multicomponent system with a greatly depressed eutectic temperature would allow for longer runouts at a given flow thickness and hence larger aspect ratios. The surface pressure on Titan is large enough to prevent vaporization of many aqueous materials contributing to longer runouts, a significant difference to the scenario modeled in this work. The low viscosity of most aqueous material makes it difficult to create flows of great thickness, channelize, and/or form levees analogous to silicate flows (cf. Kargel et al., 1991).

Given the difficulty of cryolavas eroding their substrate, these turbulent flows with intense vaporization are unlikely to be channelized like silicate flows. Instead, topographic controls would result in flows appearing more like frozen lakes, pond, or moats. On airless bodies, initial sheet flow would be unlikely to occur since the vapor pressure is so low that the liquid would immediately boil. A crust or carapace would be required in order in insulate the flow and isolate from the low-pressure environment. Thus, on icy bodies with little atmosphere, dome formation and endogenous growth (inflation) would likely be favored (Quick et al., 2017).

Additionally, residence times for cryovolcanic constructs are expected to be low (e.g., Sori et al., 2017). Viscous relaxation is faster for material with low viscosity and bodies with high gravity. However, the effect of viscosity is much greater than the effect of gravity because viscosity can change over several orders of magnitude, whereas surface gravity varies by no more than a factor of 5 across the different icy bodies in the solar system (from Ganymede at ~1.4 to Ceres and Charon at ~0.3 m s^{-2}). Water ice has a viscosity on the order of ~10^{13} Pa s at around 268 K (Jellinek & Brill, 1956). For context, the Earth's upper mantle has a viscosity approximately 6–10 orders of magnitude larger, depending on the precise temperature and depth considered (Weertman & Weertman, 1975). This suggests that the relaxation of features in the outer solar system, where ices are the dominant constituent of the surface, will be fast on a geologic time scale.

5.6. Limitations of the Current Model and Suggestions for Future Work

The model presented here represents the first attempt to couple quantitatively the thermal, chemical, and physical evolution of an effusive cryolava on an icy body. As such, there are still several inherent limitations. The current version is limited to dilute NaCl brine compositions, that is, the water-rich side of the eutectic. It is probable that eruptible material would extend to higher concentrations than we investigated here (McCord et al., 2010; Orlando et al., 2005; Vu et al., 2020). Additionally, the current version of the model is only set up to handle the H_2O-NaCl binary system. In principle, the model can easily be applied to other systems and concentration ranges, but the lack of constraints on low-temperature thermodynamic data is a practical obstacle. Thermodynamic properties like specific heat, latent heat of fusion, vapor pressure, or density of many cryovolcanically relevant compositions are very poorly constrained as a function of temperature for either the solid or the liquid phases. For example, the specific heat equations for the liquid brine (Equations 42–45) are extrapolated well outside of the calibration range. Many solutes that form these brines also crystallize hydrated minerals that may even undergo transitions to other phases or hydration states. These different species often do not have defined temperature-dependent properties that extend down to the temperatures relevant for this model. Models of other compositions will generally require more experimental determinations of thermodynamic data.

Further constraints on other physical properties are also required, such as the erodibility of ice. This model uses order of magnitude assumptions for the value of this term due to the limited laboratory data that exist to constrain

it. Understanding how the erodibility is affected by sublimation prior to inundation by the flow would also be useful. If sublimation of surface ices changes the texture of the ice or the roughness of the contact with the flow, there may be a resultant control on the friction factor or potentially the strength of the ice. Extending this work to ices with impurities or clathrates would also broaden the usefulness/applicability of this model by allowing a wider range of scenarios to be investigated. Again, further experimental studies are required.

The subliquidus rheology of aqueous systems also requires further laboratory data to constrain. The viscosity as a function of solid fraction (Costa et al., 2009) is useful because of its ability to calculate across the entire range of solid fraction, where as other models asymptotically approach a critical value. However, there are some inherent issues with the formulation such that the total, bulk solid volume fraction is essentially treated as spheres and fit to data of nonspherical grains. Recent experimental studies (Mendoza & Santamaría-Holek, 2009; Santamaría-Holek & Mendoza, 2010; e.g., Cimarelli et al., 2011; Moitra & Gonnermann, 2015) have demonstrated strong dependence of effective viscosity on size and shape distributions of suspended particles, particularly for the Einstein coefficient (B). Further studies of how size and shape distributions of particles control the rheology are required, specifically for the range of sizes and shapes expected for brine compositions.

This model is a 1D representation of flow evolution and does not portray radial/lateral evolution, nor does it strictly deal with the flow geometry (e.g., channelization). The model, in its current form, was only intended to investigate the physical state of the flow at the turbulent to laminar transition to understand the starting conditions for modeling the laminar regime.

6. Conclusions

We developed a new model for the evolution of effusive cryolava flows. This model improves upon previous efforts by linking the physical, chemical, and thermal evolution of an aqueous extrusion into a low-pressure environment. It does not rely upon the same assumptions that previous works used, like assuming laminar flow or an initial very thin icy roof. Additionally, the physical, chemical, and thermal parameters are all tracked explicitly and can be determined for any time or distance from the vent. The model is only valid for the turbulent flow regime with laminar flow under an icy roof to be dealt with separately in a future model. Understanding the state of the flow at this transition is a prerequisite for modeling the laminar regime and understanding how the flow evolves once this transition occurs.

This model was used to investigate the evolution of hypothetical H_2O-NaCl brines (5–23 wt%, 0.1–100 m thick) erupted onto a pure water-ice substrate on a Europa-like body. Results suggest that flows reach approximately 60 vol% solids at the transition from turbulent to laminar. Concentrations of 12 wt% or greater will reach the eutectic temperature for all investigated thicknesses where the temperature is buffered until complete solidification. Heat loss due to vaporization of the liquid phase is the largest heat flux for this system, accounting for >95% of the thermal budget. For hypothetical flows thicker than ~10 m, it may be useful to include frictional heating and heat loss to the eroded substrate (xenoliths), which would account for an additional 4% of the thermal budget. Our model produced broadly consistent aspect ratios for potential cryovolcanic features on Ceres and Titan but improved resolution would help identify smaller/thinner feature than may be cryovolcanic in origin.

Drawing direct comparisons to low viscosity silicate lava flows is difficult due to the orders of magnitude difference in viscosity. The active "life" of a cryolava is mainly in the turbulent regime, while that of a silicate lava is dominantly in the laminar regime (see Figure 7). Few examples exist of the type of effusive cryovolcanism presented in this model, suggesting that it is either too small to be detected with current resolution limits or is not favored due to constraints on material properties (e.g., viscosity) or simply has not been recognized. To draw comparisons between silicates and cryolavas more confidently, we would need to expand this model to cover the laminar regime, extend the 1D model to 2D or more, and acquire higher resolution imagery of the icy bodies that would allow smaller, thinner features to be resolved.

Appendix A: Formulation of Friction Factors and Reynolds Number

Throughout the literature, there is inconsistency in the formulations of friction factors, which relate to the Reynolds number. Therefore, we will take the time to summarize in more detail how we are handling these two terms. The Reynolds number is defined as the ratio of inertial forces to frictional forces within a fluid and is formulated as follows:

$$\text{Re} = \frac{Lu}{\nu} = \frac{\rho L u}{\eta} = \frac{QL}{\nu A} = \frac{WL}{\eta A} \tag{A1}$$

where L is a characteristic length, u is a mean flow velocity, ν and η are kinematic and dynamic (absolute) viscosity, respectively, A is the cross-sectional area of the flow, Q is the volumetric flow rate, and W is the mass flow rate. Occasionally, this formula is written with a four in the numerator (e.g., Wilson, Mouginis-Mark, et al., 2009; Wilson & Mouginis-Mark, 2014), which stems from the treatment of the characteristic length scale. This length scale is typically the hydraulic diameter (D_h), which is four times larger than the hydraulic radius (R_h)

$$L = D_h = 4R_h = \frac{4A}{P} \text{ (for pipe flow).} \tag{A2}$$

Hydraulic radius is defined as the cross-sectional area of the flow (A) divided by the wetted perimeter (P). The hydraulic radius is often estimated as flow thickness (h) in channelized flows. For sheet flow, the width (w) is assumed to be much larger than the thickness (depth) and the calculation of hydraulic radius reduces to only the flow thickness:

$$R_h = \frac{A}{P} = \frac{wh}{2h + w} \; if \; w \gg h, \text{ then } R_h \approx \frac{wh}{w} = h. \tag{A3}$$

When using the hydraulic radius as the characteristic length scale, it is useful to include this factor of four to maintain the same critical Reynolds numbers (transition between turbulent and laminar) as calculations using the hydraulic diameter. Different geometries or characteristic length scales affect the critical Reynolds numbers, making it difficult to directly compare different systems. Normalizing the calculation to similar critical values can aid in comparisons but should be explicitly reported and explained in detail.

The friction factor can be solved for as a function of the Reynolds number, the formulation of which differs based on whether the flow is turbulent or laminar. For laminar flow, the friction factor varies linearly:

$$f = \frac{C}{\text{Re}} \tag{A4}$$

where C is a constant, which is chosen based on the system geometry used to determine the Reynolds number. For circular pipe flow $C = 64$ and for very wide, rectangular, open channel flow, $C = 24$, where the characteristic length is the height of the vertical walls. This height (alternatively, flow depth) is analogous to the hydraulic radius. If, instead, the hydraulic diameter is used as the characteristic length scale, then $C = 96$ for the same geometry (i.e., $96 = 4*24$ because $D_h = 4R_h$ (Incropera & DeWitt, 1996; Schlichting & Gersten, 2016; White, 1999)). For turbulent flow, the Darcy-Weisbach friction factor and the Fanning friction factor are two forms of friction terms, which differ only by this factor of four that results from the use of different characteristic length scales (Incropera & DeWitt, 1996). The Darcy-Weisbach equation uses the hydraulic diameter, while the Fanning equation uses hydraulic radius, and therefore, by definition, is one fourth of the Darcy-Weisbach friction factor. The usage of one or the other is not often stated explicitly in the planetary literature; however, either can be used provided care is taken to ensure that the factor of four is appropriately considered for the length scale being used. Thus, understanding which friction factor to use is important to ensuring Re calculations are not either four times too high or low. For further discussion and a more detailed derivation of all the equations in this section, the authors point the reader to chapter six of White (1999).

Notation

Symbol	Value	Unit	Definition	Reference
A	0.64		Mean albedo	Morrison and Morrison (1977)
B	2.5		Einstein coefficient (intrinsic viscosity)	Mader et al. (2013) and Roscoe (1952)
C_1	Equation 9		Polynomial substitution for liquidus	D. L. Hall et al. (1988)
C_2	Equation 10		Polynomial substitution for liquidus	D. L. Hall et al. (1988)
C_3	Equation 24		Substitution	Costa et al. (2009)
C_4	Equation 27		Polynomial substitution for liquid viscosity	Sharqawy et al. (2010)
C_5	Equation 28		Polynomial substitution for liquid viscosity	Sharqawy et al. (2010)
C_6	Equation 42		Polynomial substitution for liquid specific heat	Millero et al. (1973)
C_7	Equation 43		Polynomial substitution for liquid specific heat	Millero et al. (1973)
D	0.001	m	Diameter of crystallizing particles	Makkonen and Tikanmäki (2018) and McFarlane et al. (2017)
E_{mech}	Equation 22	m s^{-1}	Mechanical erosion rate	Hurwitz et al. (2010)
E_v	Equation 51	m s^{-1}	Vaporization rate	Bargery and Wilson (2011) and Wilson, Bargery, and Burr (2009)
I	50.04	W m^{-2}	Incident insolation	Allison and Clifford (1987)
$L_f^{eutectic}$	223,000	J kg^{-1}	Latent heat of fusion for crystallizing eutectic mixture	Han et al. (2006)
L_f^{ice}	335,000	J kg^{-1}	Latent heat of fusion for ice	Drebushchak and Ogienko (2020) and Han et al. (2006)
L_f^{salt}	148,184	J kg^{-1}	Latent heat of fusion for non-ice eutectic crystallizing phase	Drebushchak and Ogienko (2020)
L_v	Equation 47	J kg^{-1}	Latent heat of vaporization	Bargery and Wilson (2011)
M_w	18.02e^{-3}	kg mol^{-1}	Molecular weight of the vaporizing phase	
P_a	10^{-7}	Pa	Ambient surface pressure	D. T. Hall et al. (1995)
P_{H2O}	Equation 50	Pa	Vapor pressure of water	Allison and Clifford (1987)
P_{liq}	Equation 49	Pa	Vapor pressure of the liquid brine	Nayar et al. (2016)
Q_{cond}	Equation 35	W m^{-2}	Heat flux through the base of the flow	Allison and Clifford (1987)
Q_{erod}	Equation 37	W m^{-2}	Heat flux from warming the eroded substrate	Bargery and Wilson (2011)
Q_{fric}	Equation 33	W m^{-2}	Heat flux from frictional heating	Allison and Clifford (1987)
Q_{gain}	Equation 31	W m^{-2}	Total of heat gain terms	
Q_{insol}	Equation 32	W m^{-2}	Heat flux from insolation	Allison and Clifford (1987)
Q_{loss}	Equation 31	W m^{-2}	Total of heat loss terms	
Q_{rad}	Equation 34	W m^{-2}	Heat flux from radiative cooling	Allison and Clifford (1987)
Q_{vap}	Equation 46	W m^{-2}	Heat flux from vaporization	Bargery and Wilson (2011)
ΔQ	Equation 31	W m^{-2}	Total heat flux	
R	8.314	J K^{-1} mol^{-1}	Universal gas constant	
Re_{lam}	Equation 5		Laminar Reynolds number	
Re_{turb}	Equation 3		Turbulent Reynolds number	
S	1		NaCl/(NaCl + KCl) ratio	D. L. Hall et al. (1988)
St	Equation 57		Stokes' number	
T		K	Flow temperature	
T_a	100	K	Ambient surface temperature	
T_{avg}		K	Average between the flow and substrate temperatures	

Symbol	Value	Unit	Definition	Reference
T_{eu}	252	K	Eutectic temperature	
T_{liq}	Equation 8	K	Liquidus or saturation temperature	D. L. Hall et al. (1988)
T_{sub}	273	K	Substrate melting temperature	
T_0	273	K	Starting temperature of erupted material	
ΔT	Equation 53	K	Change in temperature to be applied in the following time step	
V_{tot}	Equation 14	m^3	Total system volume	
$X(T)$	Equation 11	wt frac	Concentration of NaCl in the liquid as a function of temperature	Bodnar (1993)
$X(\varphi_{ice})$	Equation 13	wt frac	Concentration of NaCl in the liquid as a function of ice content	
X_{eu}	0.23	wt frac	Eutectic composition	
X_0		wt frac	Starting composition of the initial liquid	
Y	10^6	Pa	Strength of the substrate	Hurwitz et al. (2010) and Arvidson et al. (2004)
Z	0.94		Coefficient of evaporation	Tschudin (1946)
b_n	Table 1		Coefficients for liquid density	Sharqawy et al. (2010)
c_{bulk}	Equation 45	$J\ kg^{-1}\ K^{-1}$	Specific heat of the flow (liquid + crystals)	
c_{ice}	Equation 38	$J\ kg^{-1}\ K^{-1}$	Specific heat of ice	Ellsworth and Schubert (1983)
c_{liq}	Equation 41	$J\ kg^{-1}\ K^{-1}$	Specific heat of the liquid brine	Millero et al. (1973)
c_{salt}	Equation 39	$J\ kg^{-1}\ K^{-1}$	Specific heat of hydrohalite	Drebushchak and Ogienko (2020)
c_{NaCl}	Equation 40	$J\ kg^{-1}\ K^{-1}$	Specific heat of halite	Archer (1997)
c_w	Equation 44	$J\ kg^{-1}\ K^{-1}$	Specific heat of water	Millero et al. (1973)
d	Equation 6	m	Distance from the vent	
d_{t-1}		m	Distance from the vent at previous time step	
$dmdt^{-1}$	Equation 48	$kg\ m^{-2}\ s^{-1}$	Mass loss rate from vaporization	Kennard (1938)
e	0.001, 0.01		Erodibility of the substrate	Hurwitz et al. (2010) and Zum Gahr (1998)
f	Equation 2	–	Friction factor (Darcy-Weisbach)	
g	1.315	$m\ s^{-2}$	Gravity	
h	Equation 52	m	Flow thickness	
h_{er}	Equation 21	m	Thickness of eroded substrate material	
h_{melt}		m	Thickness of eroded and melted substrate material	
h_v	Equation 51	m	Thickness of flow lost to vaporization	
h_0		m	Initial flow thickness	
k_{ice}	Equation 36	$W\ m^{-1}\ K^{-1}$	Thermal conductivity of the substrate	Ratcliffe (1962)
t		s	Time	
Δt		s	Time step	
u_{lam}	Equation 4	$m\ s^{-1}$	Laminar velocity of the flow	
u_{turb}	Equation 1	$m\ s^{-1}$	Turbulent velocity of the flow	
z		m	Depth within the substrate	
α	0.1, 1	Degrees	Ground slope	
γ	5		Empirical fitting parameter	Mader et al. (2013)
δ	8		Empirical fitting parameter	Mader et al. (2013)
ε	0.98		Emissivity	
η_{bulk}	Equations 23 and 26	Pa s	Viscosity of the flow (liquid + crystals)	
η_{liq}	Equation 26	Pa s	Viscosity of the carrier liquid (brine)	Sharqawy et al. (2010)

Symbol	Value	Unit	Definition	Reference
η_r	Equation 23		Relative viscosity of the flow (liquid + crystals)	Costa et al. (2009)
η_w	Equation 29	Pa s	Viscosity of water	Sharqawy et al. (2010)
ξ	10^{-4}		Empirical fitting parameter	Mader et al. (2013)
ρ_{bulk}	Equation 6	kg m^{-3}	Density of the flow (liquid + crystals)	
ρ_{ice}	920	kg m^{-3}	Density of the crystallizing ice	
ρ_{liq}	Equation 7	kg m^{-3}	Density of the carrier fluid (brine)	Sharqawy et al. (2010)
ρ_{salt}	1,610	kg m^{-3}	Density of the non-ice eutectic crystallizing phase: hydrohalite	
ρ_{sub}	920	kg m^{-3}	Density of the substrate	
σ	$5.67e^{-8}$	W m^{-2} K^{-4}	Stefan-Boltzmann constant	
σ_y	Equation 31	Pa	Yield strength	Bargery and Wilson (2011)
ϕ^*	0.6	vol frac	Critical crystal volume fraction	Mader et al. (2013)
ϕ_{erod}	Equation 19	vol frac	Volume fraction of eroded solids added at a given time	
$\Sigma\phi_{erod}$	Equation 20	vol frac	Total volume fraction of eroded solids	
ϕ_{ice}	Equation 15	vol frac	Volume fraction of ice crystals	
ϕ_{salt}	Equation 16	vol frac	Volume fraction of the non-ice eutectic crystallizing phase: hydrohalite	
ϕ_{total}	Equation 25	vol frac	Total volume fraction of solids (eroded and crystallized)	
$\Sigma\phi_{xtal}$	Equation 18	vol frac	Total volume fraction of crystallized solids (as opposed to eroded solids)	
φ_{ice}	Equations 12 and 55	wt frac	Weight fraction of ice crystals	
φ_{salt}	Equation 56	wt frac	Weight fraction of the non-ice eutectic crystallizing phase: hydrohalite	
φ_{total}		wt frac	Total weight fraction of solids (eroded and crystallized)	
$\Delta\varphi_{total}$	Equation 54	wt frac	Change in total crystal content when buffered at the eutectic	
$\Sigma\varphi_{xtal}$	Equation 17	wt frac	Total weight fraction of crystallized solids (as opposed to eroded solids)	

Data Availability Statement

The calculations used to complete this work are collated in a publicly available spreadsheet (A. Morrison et al., 2022).

References

Abramov, O., & Spencer, J. R. (2008). Numerical modeling of endogenic thermal anomalies on Europa. *Icarus*, *195*(1), 378–385. https://doi.org/10.1016/j.icarus.2007.11.027

Abramov, O., & Spencer, J. R. (2009). Endogenic heat from Enceladus' south polar fractures: New observations, and models of conductive surface heating. *Icarus*, *199*(1), 189–196. https://doi.org/10.1016/j.icarus.2008.07.016

Allison, M. L., & Clifford, S. M. (1987). Ice-covered water volcanism on Ganymede. *Journal of Geophysical Research*, *92*(B8), 7865–7876. https://doi.org/10.1029/jb092ib08p07865

Archer, D. G. (1997). Enthalpy increment measurements for NaCl(cr) and KBr(cr) from 4.5 K to 350 K. Thermodynamic properties of the NaCl + H$_2$O system. 3. *Journal of Chemical & Engineering Data*, *42*(2), 281–292. https://doi.org/10.1021/je960224q

Arvidson, R. E., Anderson, R. C., Bartlett, P., Bell, J. F., Blaney, D., Christensen, P. R., et al. (2004). Localization and physical properties experiments conducted by Spirit at Gusev Crater. *Science*, *305*(5685), 821–824. https://doi.org/10.1126/science.1099922

Bargery, A. S., & Wilson, L. (2011). Erosive flood events on the surface of Mars: Application to Mangala and Athabasca Valles. *Icarus*, *212*(2), 520–540. https://doi.org/10.1016/j.icarus.2011.01.001

Beyer, R. A., Spencer, J. R., McKinnon, W. B., Nimmo, F., Beddingfield, C., Grundy, W. M., et al. (2019). The nature and origin of Charon's smooth plains. *Icarus*, *323*, 16–32. https://doi.org/10.1016/j.icarus.2018.12.036

Bodnar, R. J. (1993). Revised equation and table for determining the freezing point depression of H$_2$O-NaCl solutions. *Geochimica et Cosmochimica Acta*, *57*(3), 683–684. https://doi.org/10.1016/0016-7037(93)90378-a

Bowles, F. A., Faas, R. W., Vogt, P. R., Sawyer, W. B., & Stephens, K. (2003). Sediment properties, flow characteristics, and depositional environment of submarine mudflows, Bear Island Fan. *Marine Geology*, *197*(1–4), 63–74. https://doi.org/10.1016/s0025-3227(03)00089-6

Brenner, H. (1974). Rheology of a dilute suspension of axisymmetric Brownian particles. *International Journal of Multiphase Flow*, *1*(2), 195–341. https://doi.org/10.1016/0301-9322(74)90018-4

Britter, R. E., & Linden, P. F. (1980). The motion of the front of a gravity current travelling down an incline. *Journal of Fluid Mechanics*, *99*(3), 531–543. https://doi.org/10.1017/s0022112080000754

Byrne, P. K., Klimczak, C., Williams, D. A., Hurwitz, D. M., Solomon, S. C., Head, J. W., et al. (2013). An assemblage of lava flow features on Mercury. *Journal of Geophysical Research: Planets*, *118*(6), 1303–1322. https://doi.org/10.1002/jgre.20052

Chevrel, M. O., Baratoux, D., Hess, K.-U., & Dingwell, D. B. (2014). Viscous flow behavior of tholeiitic and alkaline Fe-rich Martian basalts. *Geochimica et Cosmochimica Acta*, *124*, 348–365. https://doi.org/10.1016/j.gca.2013.08.026

Choukroun, M., Grasset, O., Tobie, G., & Sotin, C. (2010). Stability of methane clathrate hydrates under pressure: Influence on outgassing processes of methane on Titan. *Icarus*, *205*(2), 581–593. https://doi.org/10.1016/j.icarus.2009.08.011

Cimarelli, C., Costa, A., Mueller, S., & Mader, H. M. (2011). Rheology of magmas with bimodal crystal size and shape distributions: Insights from analog experiments. *Geochemistry, Geophysics, Geosystems*, *12*(7), 1–14. https://doi.org/10.1029/2011gc003606

Clifford, S. M., & Hillel, D. (1983). The stability of ground ice in the equatorial region of Mars. *Journal of Geophysical Research*, *88*(B3), 2456. https://doi.org/10.1029/jb088ib03p02456

Cooper, J. F., Cooper, P. D., Sittler, E. C., Sturner, S. J., & Rymer, A. M. (2009). Old Faithful model for radiolytic gas-driven cryovolcanism at Enceladus. *Planetary and Space Science*, *57*(13), 1607–1620. https://doi.org/10.1016/j.pss.2009.08.002

Costa, A., Caricchi, L., & Bagdassarov, N. (2009). A model for the rheology of particle-bearing suspensions and partially molten rocks. *Geochemistry, Geophysics, Geosystems*, *10*(3), 1–13. https://doi.org/10.1029/2008gc002138

Costa, A., & Macedonio, G. (2005). Computational modeling of lava flows: A review. In M. Manga & G. V G. Soc (Eds.), *Special papers-Geological Society of America*, (Vol. *396*, pp. 209–218). Retrieved from https://www.researchgate.net/publication/230866590

Dickson, D. R., Yepsen, J. H., & Hales, J. V. (1965). Saturated vapor pressures over great salt lake brine. *Journal of Geophysical Research*, *70*(2), 500–503. https://doi.org/10.1029/jz070i002p00500

Dragoni, M. (1997). Physical modelling of lava flows. *Annales Geophysicae*, *XL*, 1179–1187.

Drebushchak, V. A., & Ogienko, A. G. (2020). Calorimetric measurements of sodium chloride dihydrate (hydrohalite). *Journal of Thermal Analysis and Calorimetry*, *140*(5), 2555–2562. https://doi.org/10.1007/s10973-019-08954-7

Eaton, J. K., & Fessler, J. R. (1994). Preferential concentration of particles by turbulence. *International Journal of Multiphase Flow*, *20*, 169–209. https://doi.org/10.1016/0301-9322(94)90072-8

Ellsworth, K., & Schubert, G. (1983). Saturn's icy satellites: Thermal and structural models. *Icarus*, *54*(3), 490–510. https://doi.org/10.1016/0019-1035(83)90242-7

Fagents, S. A. (2003). Considerations for effusive cryovolcanism on Europa: The post-Galileo perspective. *Journal of Geophysical Research*, *108*(E12), 5139. https://doi.org/10.1029/2003JE002128

Fagents, S. A., Lopes, R. M. C., Quick, L. C., & Gregg, T. K. P. (2022). Cryovolcanism. In *Planetary volcanism across the solar system* (pp. 161–234).

Fessler, J. R., Kulick, J. D., & Eaton, J. K. (1994). Preferential concentration of heavy particles in a turbulent channel flow. *Physics of Fluids*, *6*(11), 3742–3749. https://doi.org/10.1063/1.868445

Figueredo, P., Chuang, F., Rathbun, J. A., Kirk, R. L., & Greeley, R. (2002). Geology and origin of Europa's "Mitten" feature (Murias Chaos). *Journal of Geophysical Research*, *107*(E5), 1–15. https://doi.org/10.1029/2001JE001591

Fortezzo, C. M., Spudis, P. D., & Harrel, S. L. (2020). Release of the digital unified global geologic map of the moon at 1:5,000,000-scale. In *51st Lunar and Planetary Science Conference*, (p. 2760). Retrieved from https://bit.ly/LunarGeology%0Ahttps://bit.ly/LunarGeology%0Ahttp://www.lpi.usra.edu/meetings/lpsc2020/pdf/2760.pdf

Greeley, R., Fagents, S. A., Harris, R. S., Kadel, S. D., Williams, D. A., & Guest, J. E. (1998). Erosion by flowing lava: Field evidence. *Journal of Geophysical Research*, *103*(B11), 27325–27345. https://doi.org/10.1029/97jb03543

Gregg, T. K. P. (2017). Patterns and processes: Subaerial lava flow morphologies: A review. *Journal of Volcanology and Geothermal Research*, *342*, 3–12. https://doi.org/10.1016/j.jvolgeores.2017.04.022

Griffiths, R. W. (2000). The dynamics of lava flows. *Annual Review of Fluid Mechanics*, *32*(1), 477–518. https://doi.org/10.1146/annurev.fluid.32.1.477

Haber, S., & Brenner, H. (1984). Rheological properties of dilute suspensions of centrally symmetric Brownian particles at small shear rates. *Journal of Colloid and Interface Science*, *97*(2), 496–514. https://doi.org/10.1016/0021-9797(84)90322-9

Hall, D. L., Sterner, S. M., & Bodnar, R. J. (1988). Freezing point depression of NaCl-KCl-H_2O solutions. *Economic Geology*, *83*(1), 197–202. https://doi.org/10.2113/gsecongeo.83.1.197

Hall, D. T., Strobel, D. F., Feldman, P. D., Mc Grath, M. A., & Weaver, H. A. (1995). Detection of an oxygen atmosphere on Jupiter's moon Europa. *Nature*, *373*(6516), 677–679. https://doi.org/10.1038/373677a0

Han, B., Choi, J. H., Dantzig, J. A., & Bischof, J. C. (2006). A quantitative analysis on latent heat of an aqueous binary mixture. *Cryobiology*, *52*(1), 146–151. https://doi.org/10.1016/j.cryobiol.2005.09.007

Hand, K. P., & Carlson, R. W. (2015). Europa's surface color suggests an ocean rich with sodium chloride. *Geophysical Research Letters*, *42*(9), 3174–3178. https://doi.org/10.1002/2015gl063559

Hanley, T. O. D., & Tsang, G. (1984). Formation and properties of frazil in saline water. *Cold Regions Science and Technology*, *8*(3), 209–221. https://doi.org/10.1016/0165-232x(84)90052-1

Harris, A. J. L., & Rowland, S. K. (2001). FLOWGO: A kinematic thermo-rheological model for lava flowing in a channel. *Bulletin of Volcanology*, *63*(1), 20–44. https://doi.org/10.1007/s004450000120

Hori, M., Aoki, T., Tanikawa, T., Motoyoshi, H., Hachikubo, A., Sugiura, K., et al. (2006). In-situ measured spectral directional emissivity of snow and ice in the 8–14 μm atmospheric window. *Remote Sensing of Environment*, *100*(4), 486–502. https://doi.org/10.1016/j.rse.2005.11.001

Huang, X., & García, M. H. (1998). A Herschel-Bulkley model for mud flow down a slope. *Journal of Fluid Mechanics*, *374*, 305–333. https://doi.org/10.1017/s0022112098002845

Huppert, H. E., & Sparks, R. S. J. (1985). Komatiites I: Eruption and flow. *Journal of Petrology*, *26*(3), 694–725. https://doi.org/10.1093/petrology/26.3.694

Hurwitz, D. M., Fassett, C. I., Head, J. W., & Wilson, L. (2010). Formation of an eroded lava channel within an Elysium Planitia impact crater: Distinguishing between a mechanical and thermal origin. *Icarus*, *210*(2), 626–634. https://doi.org/10.1016/j.icarus.2010.07.024

Hurwitz, D. M., Head, J. W., Wilson, L., & Hiesinger, H. (2012). Origin of lunar sinuous rilles: Modeling effects of gravity, surface slope, and lava composition on erosion rates during the formation of Rima Prinz. *Journal of Geophysical Research*, *117*(E12), 1–15. https://doi.org/10.1029/2011je004000

Incropera, F. P., & DeWitt, D. P. (1996). *Introduction to heat transfer* (3rd ed.). John Wiley & Sons, Inc.

International Association for the Properties of Water and Steam. (2008). Release on the IAPWS formulation 2008 for the viscosity of ordinary water substance. Retrieved from http://www.iapws.org

Jarvis, R. A. (1995). On the cross-sectional geometry of thermal erosion channels formed by turbulent lava flows. *Journal of Geophysical Research*, *100*(B6), 10127–10140. https://doi.org/10.1029/95jb00027

Jellinek, H. H. G., & Brill, R. (1956). Viscoelastic properties of ice. *Journal of Applied Physics*, *27*(10), 1198–1209. https://doi.org/10.1063/1.1722231

Kakaç, S., Shah, R. K., & Aung, W. (1987). Handbook of single-phase convective heat transfer.

Kargel, J. S. (1991). Brine volcanism and the interior structures of asteroids and icy satellites. *Icarus*, *94*(2), 368–390. https://doi.org/10.1016/0019-1035(91)90235-l

Kargel, J. S., Croft, S. K., Lunine, J. I., & Lewis, J. S. (1991). Rheological properties of ammonia-water liquids and crystal-liquid slurries: Planetological applications. *Icarus*, *89*(1), 93–112. https://doi.org/10.1016/0019-1035(91)90090-g

Kennard, E. H. (1938). *Kinetic theory of gases* (1st ed.). McGraw-Hill.

Kerr, R. C., Griffiths, R. W., & Cashman, K. V. (2006). Formation of channelized lava flows on an unconfined slope. *Journal of Geophysical Research*, *111*(B10), 1–13. https://doi.org/10.1029/2005jb004225

Kolzenburg, S., Di Genova, D., Giordano, D., Hess, K.-U., & Dingwell, D. B. (2018). The effect of oxygen fugacity on the rheological evolution of crystallizing basaltic melts. *Earth and Planetary Science Letters*, *487*, 21–32. https://doi.org/10.1016/j.epsl.2018.01.023

Krieger, I. M., & Dougherty, T. J. (1959). A mechanism for non-Newtonian flow in suspensions of rigid spheres. *Transactions of the Society of Rheology*, *3*(1), 137–152. https://doi.org/10.1122/1.548848

Krohn, K., Jaumann, R., Stephan, K., Otto, K. A., Schmedemann, N., Wagner, R. J., et al. (2016). Cryogenic flow features on Ceres: Implications for crater-related cryovolcanism. *Geophysical Research Letters*, *43*(11), 994–12. https://doi.org/10.1002/2016GL070370

Lebofsky, L. A. (1975). Stability of frosts in the solar system. *Icarus*, *25*(2), 205–217. https://doi.org/10.1016/0019-1035(75)90020-2

Lesage, E., Massol, H., & Schmidt, F. (2020). Cryomagma ascent on Europa. *Icarus*, *335*, 113369. https://doi.org/10.1016/j.icarus.2019.07.003

Lopes, R. M. C., Kirk, R. L., Mitchell, K. L., Legall, A., Barnes, J. W., Hayes, A. G., et al. (2013). Cryovolcanism on Titan: New results from Cassini RADAR and VIMS. *Journal of Geophysical Research: Planets*, *118*(3), 416–435. https://doi.org/10.1002/jgre.20062

Lopes, R. M. C., Mitchell, K. L., Stofan, E. R., Lunine, J. I., Lorenz, R. D., Paganelli, F., et al. (2007). Cryovolcanic features on Titan's surface as revealed by the Cassini Titan Radar Mapper. *Icarus*, *186*(2), 395–412. https://doi.org/10.1016/j.icarus.2006.09.006

Mader, H. M., Llewellin, E. W., & Mueller, S. P. (2013). The rheology of two-phase magmas: A review and analysis. *Journal of Volcanology and Geothermal Research*, *257*, 135–158. https://doi.org/10.1016/j.jvolgeores.2013.02.014

Makkonen, L., & Tikanmäki, M. (2018). Modelling frazil and anchor ice on submerged objects. *Cold Regions Science and Technology*, *151*, 64–74. https://doi.org/10.1016/j.coldregions.2018.03.001

Manga, M., & Wang, C. Y. (2007). Pressurized oceans and the eruption of liquid water on Europa and Enceladus. *Geophysical Research Letters*, *34*(7), L07202. https://doi.org/10.1029/2007gl029297

McCord, T. B., Hansen, G. B., Combe, J. P., & Hayne, P. O. (2010). Hydrated minerals on Europa's surface: An improved look from the Galileo NIMS investigation. *Icarus*, *209*(2), 639–650. https://doi.org/10.1016/j.icarus.2010.05.026

McFarlane, V., Loewen, M., & Hicks, F. (2017). Measurements of the size distribution of frazil ice particles in three Alberta rivers. *Cold Regions Science and Technology*, *142*, 100–117. https://doi.org/10.1016/j.coldregions.2017.08.001

Melosh, H. J., Ekholm, A. G., Showman, A. P., & Lorenz, R. D. (2004). The temperature of Europa's subsurface water ocean. *Icarus*, *168*(2), 498–502. https://doi.org/10.1016/j.icarus.2003.11.026

Melwani Daswani, M., Vance, S. D., Mayne, M. J., & Glein, C. R. (2021). A metamorphic origin for Europa's ocean. *Geophysical Research Letters*, *48*(18), e2021GL094143. https://doi.org/10.1029/2021gl094143

Mendoza, C. I., & Santamaría-Holek, I. (2009). The rheology of hard sphere suspensions at arbitrary volume fractions: An improved differential viscosity model. *Journal of Chemical Physics*, *130*(4), 044904. https://doi.org/10.1063/1.3063120

Millero, F. J., Perron, G., & Desnoyers, J. E. (1973). Heat capacity of seawater solutions from 5° to 35°C and 0.5 to 22‰ chlorinity. *Journal of Geophysical Research*, *78*(21), 4499–4507. https://doi.org/10.1029/jc078i021p04499

Mitri, G., Showman, A. P., Lunine, J. I., & Lopes, R. M. C. (2008). Resurfacing of Titan by ammonia-water cryomagma. *Icarus*, *196*(1), 216–224. https://doi.org/10.1016/j.icarus.2008.02.024

Moitra, P., & Gonnermann, H. M. (2015). Effects of crystal shape- and size-modality on magma rheology. *Geochemistry, Geophysics, Geosystems*, *16*, 1–26. https://doi.org/10.1002/2014gc005554

Morrison, A., Whittington, A., & Mitchell, K. (2022). 1D cryolava flow model [Dataset]. Zenodo. https://doi.org/10.5281/ZENODO.7067339

Morrison, A. A., Zanetti, M. R., Hamilton, C. W., Lev, E., Neish, C. D., & Whittington, A. G. (2019). Rheological investigation of lunar highland and mare impact melt simulants. *Icarus*, *317*, 307–323. https://doi.org/10.1016/j.icarus.2018.08.001

Morrison, D., & Morrison, N. (1977). Photometry of the Galilean satellites. In J. Burns (Ed.), *Planetary satellites*, (pp. 363–378). University of Arizona Press.

Nayar, K. G., Sharqawy, M. H., Banchik, L. D., & Lienhard, J. H. (2016). Thermophysical properties of seawater: A review and new correlations that include pressure dependence. *Desalination*, *390*, 1–24. https://doi.org/10.1016/j.desal.2016.02.024

Orlando, T. M., McCord, T. B., & Grieves, G. A. (2005). The chemical nature of Europa surface material and the relation to a subsurface ocean. *Icarus*, *177*(2), 528–533. https://doi.org/10.1016/j.icarus.2005.05.009

Parsons, J. D., Whipple, K. X., & Simoni, A. (2001). Experimental study of the grain flow, fluid-mud transition in debris flows. *The Journal of Geology*, *109*(4), 427–447. https://doi.org/10.1086/320798

Peterson, D. W., Holcomb, R. T., Holcomb, R. T., Tilling, R. I., & Christiansen, R. L. (1994). Development of lava tubes in the light of observations at Mauna Ulu, Kilauea Volcano, Hawaii. *Bulletin of Volcanology*, *56*(5), 343–360. https://doi.org/10.1007/bf00326461

Poston, M. J., Carlson, R. W., & Hand, K. P. (2017). Spectral behavior of irradiated sodium chloride crystals under Europa-like conditions. *Journal of Geophysical Research: Planets*, *122*(12), 2644–2654. https://doi.org/10.1002/2017je005429

Quick, L. C., Buczkowski, D. L., Ruesch, O., Scully, J. E. C., Castillo-Rogez, J., Raymond, C. A., et al. (2019). A possible brine reservoir beneath Occator crater: Thermal and compositional evolution and formation of the Cerealia dome and Vinalia Faculae. *Icarus*, *320*, 119–135. https://doi.org/10.1016/j.icarus.2018.07.016

Quick, L. C., Glaze, L. S., & Baloga, S. M. (2017). Cryovolcanic emplacement of domes on Europa. *Icarus*, *284*, 477–488. https://doi.org/10.1016/j.icarus.2016.06.029

Rallison, J. M. (1978). The effects of Brownian rotations in a dilute suspension of rigid particles of arbitrary shape. *Journal of Fluid Mechanics*, *84*(02), 237–263. https://doi.org/10.1017/s0022112078000142

Ratcliffe, E. H. (1962). The thermal conductivity of ice new data on the temperature coefficient. *Philosophical Magazine*, *7*(79), 1197–1203. https://doi.org/10.1080/14786436208209120

Reeks, M. W. (2014). Transport, mixing and agglomeration of particles in turbulent flows. *Journal of Physics: Conference Series*, *530*, 012003. https://doi.org/10.1088/1742-6596/530/1/012003

Roberts, C. E., & Gregg, T. K. P. (2019). Rima Marius, the Moon: Formation of lunar sinuous rilles by constructional and erosional processes. *Icarus*, *317*, 682–688. https://doi.org/10.1016/j.icarus.2018.02.033

Roscoe, R. (1952). The viscosity of suspensions of rigid spheres. *British Journal of Applied Physics*, *3*(8), 267–269. https://doi.org/10.1088/0508-3443/3/8/306

Roth, L., Saur, J., Retherford, K. D., Strobel, D. F., Feldman, P. D., McGrath, M. A., & Nimmo, F. (2014). Transient water vapor at Europa's south pole. *Science*, *343*(6167), 171–174. https://doi.org/10.1126/science.1247051

Ruesch, O., Platz, T., Schenk, P. M., McFadden, L. A., Castillo-Rogez, J. C., Quick, L. C., et al. (2016). Cryovolcanism on Ceres. *Science*, *353*(6303), aaf4286. https://doi.org/10.1126/science.aaf4286

Ruesch, O., Quick, L. C., Landis, M. E., Sori, M. M., Čadek, O., Brož, P., et al. (2019). Bright carbonate surfaces on Ceres as remnants of salt-rich water fountains. *Icarus*, *320*, 39–48. https://doi.org/10.1016/j.icarus.2018.01.022

Santamaría-Holek, I., & Mendoza, C. I. (2010). The rheology of concentrated suspensions of arbitrarily-shaped particles. *Journal of Colloid and Interface Science*, *346*(1), 118–126. https://doi.org/10.1016/j.jcis.2010.02.033

Sauro, F., Pozzobon, R., Massironi, M., De Berardinis, P., Santagata, T., & De Waele, J. (2020). Lava tubes on Earth, Moon and Mars: A review on their size and morphology revealed by comparative planetology. *Earth-Science Reviews*, *209*, 103288. https://doi.org/10.1016/j.earscirev.2020.103288

Schlichting, H., & Gersten, K. (2016). Boundary-layer theory.

Sehlke, A., & Whittington, A. G. (2015). Rheology of lava flows on Mercury: An analog experimental study. *Journal of Geophysical Research: Planets*, *120*(11), 1924–1955. https://doi.org/10.1002/2015je004792

Sehlke, A., Whittington, A. G., Robert, B., Harris, A. J. L., Gurioli, L., & Médard, E. (2014). Pahoehoe toáá transition of Hawaiian lavas: An experimental study. *Bulletin of Volcanology*, *76*, 1–20. https://doi.org/10.1007/s00445-014-0876-9

Sharqawy, M. H., Lienhard, V. J. H., & Zubair, S. M. (2010). Thermophysical properties of seawater: A review of existing correlations and data. *Desalination and Water Treatment*, *16*(1–3), 354–380. https://doi.org/10.5004/dwt.2010.1079

Showman, A. P., Mosqueira, I., & Head, J. W. (2004). On the resurfacing of Ganymede by liquid – water volcanism. *Icarus*, *172*(2), 625–640. https://doi.org/10.1016/j.icarus.2004.07.011

Sklar, L. S., & Dietrich, W. E. (1998). River longitudinal profiles and bedrock incision models: Stream power and the influence of sediment supply. *Geophysical Monograph-American Geophysical Union*, *107*, 237–260.

Sklar, L. S., & Dietrich, W. E. (2001). Sediment and rock strength controls on river incision into bedrock. *Geology*, *29*(12), 1087–1090. https://doi.org/10.1130/0091-7613(2001)029<1087:sarsco>2.0.co;2

Sori, M. M., Byrne, S., Bland, M. T., Bramson, A. M., Ermakov, A. I., Hamilton, C. W., et al. (2017). The vanishing cryovolcanoes of Ceres. *Geophysical Research Letters*, *44*(3), 1243–1250. https://doi.org/10.1002/2016gl072319

Sparks, W. B., Schmidt, B. E., McGrath, M. A., Hand, K. P., Spencer, J. R., Cracraft, M., & Deustua, S. E. (2017). Active cryovolcanism on Europa? *The Astrophysical Journal*, *839*(2), L18. https://doi.org/10.3847/2041-8213/aa67f8

Spencer, J. R., Barr, A. C., Esposito, L. W., Helfenstein, P., Ingersoll, A. P., Jaumann, R., et al. (2009). Enceladus: An active cryovolcanic satellite. In *Saturn from Cassini-Huygens* (pp. 683–724).

Sterner, S. M., Hall, D. L., & Bodnar, R. J. (1988). Synthetic fluid inclusions. V. Solubility relations in the system NaCl-KCl-H_2O under vapor-saturated conditions. *Geochimica et Cosmochimica Acta*, *52*(5), 989–1005. https://doi.org/10.1016/0016-7037(88)90254-2

Stickler, M., & Alfredsen, K. T. (2009). Anchor ice formation in streams: A field study. *Hydrological Processes*, *23*(16), 2307–2315. https://doi.org/10.1002/hyp.7349

Thomas, E. C., Vu, T. H., Hodyss, R., Johnson, P. V., & Choukroun, M. (2019). Kinetic effect on the freezing of ammonium-sodium-carbonate-chloride brines and implications for the origin of Ceres' bright spots. *Icarus*, *320*, 150–158. https://doi.org/10.1016/j.icarus.2017.12.038

Tobie, G., Lunine, J. I., & Sotin, C. (2006). Episodic outgassing as the origin of atmospheric methane on Titan. *Nature*, *440*(7080), 61–64. https://doi.org/10.1038/nature04497

Tsang, G. (1982). *Frazil and anchor ice: A monograph*. National Research Council Canada, Subcommittee Hydraul Ice Cover.

Tsang, G., & Hanley, T. O. (1985). Frazil formation in water of different salinities and supercoolings. *Journal of Glaciology*, *31*(108), 74–85. https://doi.org/10.3189/s0022143000006298

Tschudin, K. (1946). Rate of evaporation of ice. *Helvetica Physica Acta*, *19*, 91–102.

Valerio, A., Tallarico, A., & Dragoni, M. (2008). Mechanisms of formation of lava tubes. *Journal of Geophysical Research*, *113*(B8), B08209. https://doi.org/10.1029/2007jb005435

Vu, T. H., Choukroun, M., Hodyss, R., & Johnson, P. V. (2020). Probing Europa's subsurface ocean composition from surface salt minerals using in-situ techniques. *Icarus*, *349*, 113746. https://doi.org/10.1016/j..icarus.2020.113746

Wakiya, S. (1971). Slow motion in shear flow of a doublet of two spheres in contacts. *Journal of the Physical Society of Japan*, *31*(5), 1581–1587. https://doi.org/10.1143/jpsj.31.1581

Washburn, E. W., Hull, C., & West, C. J. (1926). *Phase equilibrium data*. International Critical Tables of Numerical Data, Physics, Chemistry and Technology.

Weertman, J., & Weertman, J. R. (1975). High temperature creep of rock and mantle viscosity. *Annual Review of Earth and Planetary Sciences*, *3*(1), 293–315. https://doi.org/10.1146/annurev.ea.03.050175.001453

Whipple, K. X. (2004). Bedrock rivers and the geomorphology of active orogens. *Annual Review of Earth and Planetary Sciences*, *32*(1), 151–185. https://doi.org/10.1146/annurev.earth.32.101802.120356

Whipple, K. X., Hancock, G. S., & Anderson, R. S. (2000). River incision into bedrock: Mechanics and relative efficacy of plucking, abrasion, and cavitation. *Bulletin of the Geological Society of America*, *112*(3), 490–503. https://doi.org/10.1130/0016-7606(2000)112<490:riibma>2.0.co;2

White, F. M. (1999). *Fluid mechanics* (4th ed.). McGraw-Hill.

Williams, D. A., Fagents, S. A., & Greeley, R. (2000). A reassessment of the emplacement and erosional potential of turbulent, low-viscosity lavas on the Moon. *Journal of Geophysical Research*, *105*(E8), 20189–20205. https://doi.org/10.1029/1999je001220

Williams, D. A., Greeley, R., Lopes, R. M. C., & Davies, A. G. (2001). Evaluation of sulfur flow emplacement on Io from Galileo data and numerical modeling. *Journal of Geophysical Research*, *106*(E12), 33161–33174. https://doi.org/10.1029/2000je001340

Wilson, L., Bargery, A. S., & Burr, D. M. (2009). Dynamics of fluid flow in Martian outflow channels. *Megaflooding Earth Mars*, 290–311.

Wilson, L., Head, J. W., & Pappalardo, R. T. (1997). Eruption of lava flows on Europa: Theory and application to Thrace Macula. *Journal of Geophysical Research*, *102*(E4), 9263–9272. https://doi.org/10.1029/97je00412

Wilson, L., & Mouginis-Mark, P. J. (2014). Dynamics of a fluid flow on Mars: Lava or mud? *Icarus*, *233*, 268–280. https://doi.org/10.1016/j.icarus.2014.01.041

Wilson, L., Mouginis-Mark, P. J., Tyson, S., Mackown, J., & Garbeil, H. (2009). Fissure eruptions in Tharsis, Mars: Implications for eruption conditions and magma sources. *Journal of Volcanology and Geothermal Research*, *185*(1–2), 28–46. https://doi.org/10.1016/j.jvolgeores.2009.03.006

Wylie, J. J., Helfrich, K. R., Dade, B., Lister, J. R., & Salzig, J. F. (1999). Flow localization in fissure eruptions. *Bulletin of Volcanology*, *60*(6), 432–440. https://doi.org/10.1007/s004450050243

Zhang, L., Jebakumar, A. S., & Abraham, J. (2016). Lattice Boltzmann method simulations of Stokes number effects on particle motion in a channel flow. *Physics of Fluids*, *28*(6), 063306. https://doi.org/10.1063/1.4953800

Zum Gahr, K. H. (1998). Wear by hard particles. *Tribology International*, *31*(10), 587–596. https://doi.org/10.1016/s0301-679x(98)00079-6